RADIO SCIENCE, VOL. 40, RS1007, doi:10.1029/2004RS003110, 2005

Intercomparison of general purpose clear sky atmospheric radiative transfer models for the millimeter/submillimeter spectral range

C. Melsheimer,[1] C. Verdes,[1] S. A. Buehler,[1] C. Emde,[1] P. Eriksson,[2] D. G. Feist,[3] S. Ichizawa,[4] V. O. John,[1] Y. Kasai,[5] G. Kopp,[6] N. Koulev,[1] T. Kuhn,[1] O. Lemke,[1] S. Ochiai,[5] F. Schreier,[7] T. R. Sreerekha,[1] M. Suzuki,[4] C. Takahashi,[8] S. Tsujimaru,[4,9] and J. Urban[10,11]

Received 16 June 2004; revised 17 September 2004; accepted 16 November 2004; published 15 February 2005.

[1] We compare a number of radiative transfer models for atmospheric sounding in the millimeter and submillimeter wavelength range, check their consistency, and investigate their deviations from each other. This intercomparison deals with three different aspects of radiative transfer models: (1) the inherent physics of gaseous absorption lines and how they are modeled, (2) the calculation of absorption coefficients, and (3) the full calculation of radiative transfer for different geometries, i.e., up-looking, down-looking, and limb-looking. The correctness and consistency of the implementations are tested by comparing calculations with predefined input such as spectroscopic data, line shape, continuum absorption model, and frequency grid. The absorption coefficients and brightness temperatures calculated by the different models are generally within about 1% of each other. Furthermore, the variability or uncertainty of the model results is estimated if (except for the atmospheric scenario) the input such as spectroscopic data, line shape, and continuum absorption model could be chosen freely. Here the models deviate from each other by about 10% around the center of major absorption lines. The main cause of such discrepancies is the variability of reported spectroscopic data for line absorption and of the continuum absorption model. Further possible causes of discrepancies are different frequency and pressure grids and differences in the corresponding interpolation routines, as well as differences in the line shape functions used, namely a prefactor of (ν/ν_0) or $(\nu/\nu_0)^2$ of the Van-Vleck-Weisskopf line shape function. Whether or not the discrepancies affect retrieval results remains to be investigated for each application individually.

Citation: Melsheimer, C., et al. (2005), Intercomparison of general purpose clear sky atmospheric radiative transfer models for the millimeter/submillimeter spectral range, *Radio Sci.*, *40*, RS1007, doi:10.1029/2004RS003110.

1. Introduction

[2] During the past decades, numerous atmospheric radiative transfer models have been developed, i.e., computer programs that simulate the radiative transfer in the atmosphere. Most of them have been developed for specific purposes, typically for the analysis of data

0048-6604/05/2004RS003110$11.00

---

[1] Institute of Environmental Physics, University of Bremen, Bremen, Germany.

[2] Department of Radio and Space Science, Chalmers University of Technology, Göteborg, Sweden.

[3] Institute of Applied Physics, University of Bern, Bern, Switzerland.

[4] Earth Observation Research and Application Center (EORC), Japan Aerospace Exploration Agency (JAXA), Tokyo, Japan.

[5] National Institute of Information and Communications Technology (NICT), Tokyo, Japan.

[6] Institute of Meteorology and Climate Research, Forschungszentrum Karlsruhe GmbH, Karlsruhe, Germany.

[7] German Aerospace Center (DLR), Remote Sensing Technology Institute, Oberpfaffenhofen, Germany.

[8] Fujitsu FIP Corporation, Environmental System Business Division, Tokyo, Japan.

[9] Now at National Institute of Information and Communications Technology (NICT), Tokyo, Japan.

[10] Observatoire de Bordeaux, Floirac, France.

[11] Now at Department of Radio and Space Science, Chalmers University of Technology, Göteborg, Sweden.

from specific sensors. Therefore they are typically suitable for, e.g., a limited wavelength range, or for a specific geometry as relevant for the sensor.

[3] Such models (commonly called "forward models") are used to simulate the intensity of radiation that a sensor would measure for a given state of the atmosphere (pressure, temperature, constituent gases) and a given source of the radiation. The simulations are needed, e.g., when developing and designing new sensors, when retrieving atmospheric parameters (e.g., temperature, trace gas concentrations) from actual measurements, or when correcting measurements of the radiation from earth or space for the influence and contribution of the atmosphere.

[4] The aim of this paper is (1) to compare a number of forward models developed independently for atmospheric sounding, applicable in the millimeter and submillimeter wavelength range and for different geometries, including limb-looking, and (2) to check their consistency and investigate their deviations from each other. Similar recent intercomparison studies are *Tjemkes et al.* [2003], *von Clarmann et al.* [2003b], *Garand et al.* [2001]. However, the studies by *von Clarmann et al.* [2003b] and *Tjemkes et al.* [2003] focused on the infrared wavelength range, and the study by *Garand et al.* [2001] focused exclusively on models for the Advanced Television Infrared Observation Satellite (TIROS) Operational Vertical Sounder (ATOVS) instruments flown on polar orbiting meteorological satellites (POES) of NASA.

[5] Section 2 reviews the basic equations relevant for this intercomparison study, sections 3 and 4 briefly present the forward models that participated in this study and the setup of this study. The subsequent sections deal with three different aspects of the radiative transfer models on which this study focuses: (1) the inherent physics of gaseous absorption lines and how they are modeled (section 5), (2) the calculation of absorption coefficients (section 6), and (3) the full calculation of radiative transfer for different geometries, i.e., down-looking, limb-looking, and up-looking (section 7). Section 8 points out what has been learned not only by the results of this study, but also from performing it; section 9 gives a brief summary. Appendix A gives details about the radiative transfer models that participated in this study.

2. Basic Equations

[6] Before going into the details of this intercomparison study, let us give a brief overview of the basic equations related to radiative transfer in the atmosphere in the millimeter and submillimeter wave domain. More details and derivations can be found in books by authors like, e.g., *Goody and Yung* [1989] or *Janssen* [1993].

[7] The radiation field is described in terms of the specific intensity I_ν, which is defined as the flux of energy in a given direction per second at a given frequency (ν) per unit frequency interval per unit solid angle per unit area.

[8] In the case of microwaves, scattering by air molecules is negligible (as compared to absorption), scattering by aerosols can be neglected as well, and scattering by cloud particles (droplets, ice particles) is neglected here since we only consider clear sky. In the case of local thermodynamic equilibrium, the integral form of the radiative transfer equation is then given by

$$I_\nu(0) = \int_0^{s_{\mathrm{bg}}} \alpha_\nu(s)\, B_\nu(T(s))\, \mathrm{e}^{-\tau_\nu(s)}\, \mathrm{d}s + I_\nu\left(s_{\mathrm{bg}}\right) \mathrm{e}^{-\tau_\nu\left(s_{\mathrm{bg}}\right)} \tag{1}$$

where s is the coordinate along the line of sight; the observer (e.g., a radiometer) is at $s = 0$, the background is at $s = s_{\mathrm{bg}}$ and contributes the background radiation $I_\nu(s_{\mathrm{bg}})$. For up-looking and limb-looking geometry, $s_{\mathrm{bg}} = \infty$ and $I_\nu(s_{\mathrm{bg}})$ usually is the cosmic background, whereas for down-looking geometry, s_{bg} is finite and $I_\nu(s_{\mathrm{bg}})$ is the radiation emitted by the ground. The α_ν is the absorption coefficient, $\tau_\nu(s)$ is the opacity defined as

$$\tau_\nu(s) = \int_0^{s} \alpha_\nu(s')\, \mathrm{d}s' \tag{2}$$

and $B_\nu(T)$ is the Planck function defined as

$$B_\nu(T) = \frac{2h\nu^3}{c^2} \frac{1}{\mathrm{e}^{h\nu/kT} - 1} \tag{3}$$

Here, h is Planck's constant, c is the speed of light, k is Boltzmann's constant, and T is the physical temperature. The integral in equation (1) can be easily evaluated numerically, provided the absorption coefficient is known.

[9] The absorption coefficient α_ν for a specific gas absorption line can be written as

$$\alpha_\nu = n\, S(T)\, F(\nu) \tag{4}$$

where n is the number density of the absorber molecule, $S(T)$ is the line strength and $F(\nu)$ is the line shape function ($\int F(\nu)\, d\nu = 1$). Spectroscopic databases (also called spectral line catalogs) contain the value of S at a reference temperature T_0 for each spectral line. The conversion to other temperatures is done according to [*Pickett et al.*, 1992]

$$S(T) = S(T_0)\, \frac{Q(T_0)}{Q(T)}\, \frac{\mathrm{e}^{-E_l/kT}\left(1 - \mathrm{e}^{-h\nu_0/kT}\right)}{\mathrm{e}^{-E_l/kT_0}\left(1 - \mathrm{e}^{-h\nu_0/kT_0}\right)} \tag{5}$$

where E_l is the lower energy level of the states between which the transition occurs, ν_0 is the transition frequency, and $Q(T)$ is the partition function. Spectral line catalogs contain E_l tabulated along with ν_0 and $S(T_0)$. Partition functions $Q(T)$ for all molecular species are also available along with some spectral line catalogs, either in the form of tabulated values for a set of temperatures, or as polynomial approximations.

[10] In order to determine the line shape function $F(\nu)$ of atmospheric absorption lines, two effects have to be considered: Doppler or thermal broadening and collisional or pressure broadening. Doppler broadening is caused by the thermal motion of the gas molecules. Collisional broadening is caused by a perturbation of the energy levels by collisions of the molecules.

[11] Doppler broadening is dominant in the upper stratosphere and mesosphere for microwave frequencies. The Doppler line shape function is

$$F_{\mathrm{D}}(\nu,\nu_0) = \frac{1}{\gamma_{\mathrm{D}}\sqrt{\pi}} \exp\left[-\left(\frac{\nu-\nu_0}{\gamma_{\mathrm{D}}}\right)^2\right] \tag{6}$$

where $\gamma_{\mathrm{D}} = \frac{\nu_0}{c}\sqrt{\frac{2kT}{m}}$. Here ν_0 is the line center frequency, and m the mass of the respective molecule. The Doppler line shape is just a Gaussian, with the Doppler width γ_{D} giving the half width at 1/e maximum of the line shape function.

[12] Collisional broadening is more complicated than Doppler broadening. So far, it is not possible to calculate from basic principles a collisional line shape that is valid near the line center and in the far wing. All theoretical line shapes must rely on approximations that limit them to certain regions of the line profile. The most popular of these approximations is the impact approximation which states that the duration of the collisions is short compared to the time between collisions. That approximation allows the formulation of a simplified kinetic theory which yields the Lorentz line shape

$$F_{\mathrm{L}}(\nu,\nu_0) = \frac{\gamma_{\mathrm{L}}}{\pi}\frac{1}{(\nu-\nu_0)^2+\gamma_{\mathrm{L}}^2} \tag{7}$$

where γ_{L} is the Lorentz line width which is a function of pressure and temperature. A generalization of the Lorentz line shape particularly for the microwave spectral region is the van Vleck-Weisskopf line shape [*Van Vleck and Weisskopf*, 1945]

$$F_{\mathrm{VVW}}(\nu,\nu_0) = \left(\frac{\nu}{\nu_0}\right)^2 [F_{\mathrm{L}}(\nu,\nu_0) + F_{\mathrm{L}}(\nu,-\nu_0)] \tag{8}$$

which reduces to the Lorentz line shape for $|\nu - \nu_0| \ll \nu_0$. Note that this line shape function is an approximation and is not normalized [*Rayer*, 2001].

[13] Collision and Doppler broadening are taken into account simultaneously by the Voigt line shape, a convolution of the Lorentz line shape with a Doppler line shape:

$$F_{\mathrm{Voigt}}(\nu,\nu_0) = \int F_{\mathrm{L}}(\nu,\nu')\,F_{\mathrm{D}}(\nu',\nu_0)\,d\nu' \tag{9}$$

This line shape is an approximation of the true line shape in the transition regime where both collisional broadening and Doppler broadening are significant. There is no analytical solution to the integral in equation (9), so one of several available approximation algorithms has to be used (see survey in the work of *Schreier* [1992]).

[14] Finally, one can implement a hybrid line shape that behaves like a Van Vleck-Weisskopf line shape in the high pressure limit and like a Voigt line shape in the low pressure limit:

$$F_{\mathrm{Hybrid}}(\nu,\nu_0) = \left(\frac{\nu}{\nu_0}\right)^2 \left[F_{\mathrm{Voigt}}(\nu,\nu_0) + F_{\mathrm{Voigt}}(\nu,-\nu_0)\right] \tag{10}$$

[15] Not related to the physics, but rather to the modeling of radiative transfer, is the way how to discretize functions of the vertical spatial variable (height h). Instead of taking point values at discrete heights, weighted means over layers can be taken, so-called Curtis-Godson means. The Curtis-Godson mean of a quantity X (e.g., pressure, temperature, or some volume mixing ratio) for layer j (between h_j and h_{j+1}) is defined by

$$X_j = \frac{\displaystyle\int_{h_j}^{h_{j+1}} X(h')n(h')\,\mathrm{d}h'}{\displaystyle\int_{h_j}^{h_{j+1}} n(h')\,\mathrm{d}h'} \tag{11}$$

where $n(h')$ is the number density of the atmosphere's molecules as a function of height h', and $X(h')$ is the said physical quantity (e.g., pressure, temperature, or some volume mixing ratio) as a function of height h'.

3. Participating Models

[16] The forward models which participated in this intercomparison study were as follows.

[17] 1. Atmospheric Radiative Transfer Simulator (ARTS), a public domain project which was initiated and developed jointly by the University of Bremen, Germany, and Chalmers University, Göteborg, Sweden [*Buehler et al.*, 2005]. ARTS is used for the retrieval of atmospheric parameters from data from the limb sounder

Table 1. Main Features of the Participating Radiative Transfer Models[a]

Model	Catalog[b]	Partition Function[c]	Line Shape[d]	Continuum Absorption[e]	Refraction[f]	Geometry[g]
ARTS	J, H, O	poly.	Hy, Vo, VVW, Lo, Do	CKD, MPM, PWR, O	yes	D,L,U
BEAM	J, H, O	JPL/int.	Vo, VVW	MPM93	no	L,U
EORC	J, H	JPL/int., O	Vo, VVW, Lo, Do	MPM89,93	yes	D,L,U
KMM[h]	H	O	VVW	MPM89	yes	U
MAES	J, H	JPL/int.	Vo, Lo, Do	MPM89,93	no	D,L,U
MIRART	J, H, O	O	Hy, Vo, Lo	CKD2.2, O	yes	D,L,U
MOLIERE/5	J, H, O	poly.	Hy, Vo, VVW, Lo, O	CKD,MPM93	yes	D,L,U
SMOCO	J, H	JPL/int.	Vo, Lo, Do	MPM89,93	yes	D,L

[a] For details and references on the models, see section 3 and Appendix A.

[b] The spectral line catalog used, "J" is the JPL line catalog [*Pickett et al.*, 1998], "H" is the HITRAN line catalog [*Rothman et al.*, 1998], and "O" is others (for details, see model descriptions in Appendix A).

[c] Approach to calculate the partition function used in the temperature conversion of the line strength. "Poly." is a polynomial in T (temperature), "JPL/int." is interpolation between values given in the JPL line catalog, and "O" is other approach (for details, see Appendix A).

[d] Line shape function used for the line absorption. "Hy" is the hybrid line shape function as defined in equation (10), "Vo" is Voigt (cf. equation (9)), "VVW" is Van Vleck–Weisskopf (cf. equation (8)), "Lo" is Lorentz (cf. equation (7)), and "Do" is Doppler (cf. equation (6)).

[e] The model used for continuum absorption. CKD is the Clough-Kneizys-Davies model [*Clough et al.*, 1989], MPM89 and MPM93 are the models by *Liebe* [1989] and *Liebe et al.* [1993], respectively, and PWR is the model by *Rosenkranz* [1993, 1998].

[f] The inclusion of the effect of atmospheric refraction.

[g] The types of viewing geometry that can be handled. "D" is down-looking, "L" is limb-looking, and "U" is up-looking.

[h] Note that KMM does not model antenna response and channel response, i.e., it uses pencil beams.

on board the Odin satellite, from the Advanced Microwave Sounding Unit (AMSU) on board the NOAA polar-orbiting satellites, and from the ground-based Radiometer for Atmospheric Measurements (RAM) and the airborne Airborne Submillimeter Radiometer (ASUR) instruments. ARTS has further been used for instrument studies of Superconductive Submillimeter Limb Emission Sounder (SMILES) and Millimeter-Wave Acquisitions for Stratosphere/Troposphere Exchange Research/Submillimeter Observation of Processes in the Atmosphere Noteworthy for Ozone (MASTER/SOPRANO).

[18] 2. Bernese Atmospheric Model (BEAM), developed at the Institute of Applied Physics (IAP), University of Bern, Switzerland [*Feist*, 2001; *Feist and Kämpfer*, 1998; *Feist*, 1999a]. Today, BEAM is used for the data analysis of all the radiometric instruments at IAP as well as the ozone radiometer SOMORA at MeteoSwiss.

[19] 3. Earth Observation Research Center (EORC) model developed at EORC, National Space Development Agency (NASDA), Japan (for details see Table 1 and Appendix A). It is mainly intended as accurate and numerically efficient software for the L2 data processing of the planned Superconductive Submillimeter Limb Emission Sounder (SMILES) to be aboard the Japanese Experiment Module (JEM) of the International Space Station (ISS).

[20] 4. Karlsruhe Millimeter-Wave Forward Model (KMM) developed for ground-based millimeter-wave radiometry at the Forschungszentrum Karlsruhe, Germany [*Kopp*, 2001]. It was used for the retrieval of ozone volume mixing ratio profiles from measurements of a 142 GHz radiometer and for the retrieval of ozone, ClO, HNO_3 and N_2O profiles from measurements of the 268–280 GHz radiometer of the Forschungszentrum Karlsruhe. Since winter 2001/2002, the model has also been used for profile retrieval of the 200–228 GHz radiometer of the Swedish Institute of Space Physics (Institutet för Rymdfysik (IRF)) in Kiruna.

[21] 5. Millimeter Wave Atmospheric Emission Simulator (MAES), developed at the Communications Research Laboratory (CRL, now National Institute of Information and Communications Technology (NICT)), Tokyo, Japan (for details see Table 1 and Appendix A). MAES has been applied to data analyses of CRL ground-based millimeter-wave radiometers [*Ochiai et al.*, 2001] and to designing of the CRL Balloonborne Superconducting Submillimeter-Wave Limb-Emission Sounder (BSMILES) [*Irimajiri et al.*, 2002] and space station–borne SMILES [*SMILES Mission Team*, 2002].

[22] 6. Modular Infrared Atmospheric Radiative Transfer (MIRART) developed at the Remote Sensing Technology Institute of the German Aerospace Center, Deutsches Zentrum für Luft- und Raumfahrt (DLR) [*Schreier and Schimpf*, 2001; *Schreier and Böttger*, 2003]. It is used, e.g., for data analysis of the Michelson Interferometer for Passive Atmospheric Sounding (MIPAS) and for far-infrared heterodyne spectroscopy of the stratosphere.

[23] 7. Microwave Observation Line Estimation and Retrieval Code, Version 5 (MOLIERE/5) developed at the Observatoire de Bordeaux, France [*Urban et al.*, 2004]. MOLIERE/5 is implemented in version 223 of the data processor used for the retrieval of vertical

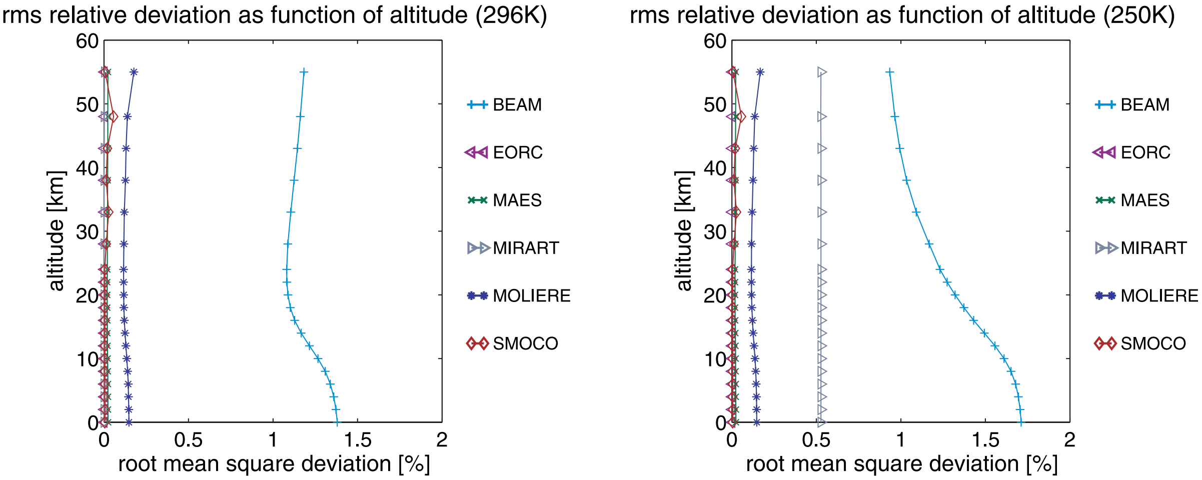

Figure 1. Exercise 0. Root mean square relative deviation of the participating models from ARTS (in percent) as a function of altitude. Temperatures: (left) 296 K and (right) 250 K.

constituent profiles from limb observations of the submillimeter radiometer (SMR) on board the Odin satellite.

[24] 8. SMILES Observation Retrieval Code (SMOCO) developed by CRL (now NICT) in collaboration with Fujitsu FIP Corporation, Tokyo, Japan [*SMILES Mission Team*, 2002]. The main purpose of this model is to retrieve altitude profiles of molecular concentrations and of temperature from spectra measured by JEM/SMILES. SMOCO is the official retrieval code for the SMILES ground segment system for L1 and L2 processing.

[25] The main features and capabilities of the models are summarized in Table 1. Further relevant details are given in Appendix A.

4. Intercomparison Setup

[26] The intercomparison was carried out in five “exercises” that can be grouped into three parts, according to the aspect of radiative transfer modeling on which they focus. The first part (exercise 0) deals with a check of the line shape function (see section 5). The second part (exercise 1 and exercise 2) deals with a comparison of the absorption coefficients calculation (see section 6). The third part (exercise 3 and exercise 4) concerns the radiative transfer (see section 7). Exercise 0, exercise 1 and exercise 3 are calculations with a fully specified set of input parameters, with the purpose of making a direct comparison of the model implementations. Exercise 2 and exercise 4 are calculations where only some input parameters are common and the remaining ones are to be set by the participants. These latter exercises are meant to test the absolute uncertainties that are present in the calculations (including uncertainties in input parameters).

5. Line Shape Implementation Test (Exercise 0)

[27] The purpose of this exercise is to test the implementation of the Voigt line shape function. More precisely, the prescribed line shape for this exercise was the Voigt line shape with a quadratic prefactor:

$$F_{\mathrm{Ex.0}}(\nu, \nu_0) = \left(\frac{\nu}{\nu_0}\right)^2 F_{\mathrm{Voigt}}(\nu, \nu_0) \qquad (12)$$

[28] This was an arbitrary decision for the intercomparison, not a judgment that this is the best line shape to use. Other reasonable choices would have been the pure Voigt line shape of equation (9), or the hybrid line shape of equation (10). For the low frequency bands, the hybrid line shape would have been a more realistic choice, but it is not supported by most models except ARTS and MIRART. Note that KMM does not support the Voigt line shape, therefore this model could not participate in this exercise.

5.1. Calculations (Exercise 0)

[29] The absorption coefficient was calculated for just one line, the ozone line at 110.83 GHz, but for various pressure levels corresponding to altitudes between 0 and 55 km. Spectroscopic parameters were taken from the HITRAN line catalog. Two sets of calculations were carried out: (1) for constant temperature T = 296 K, chosen because the HITRAN line catalog provides line intensities for this temperature and (2) for constant

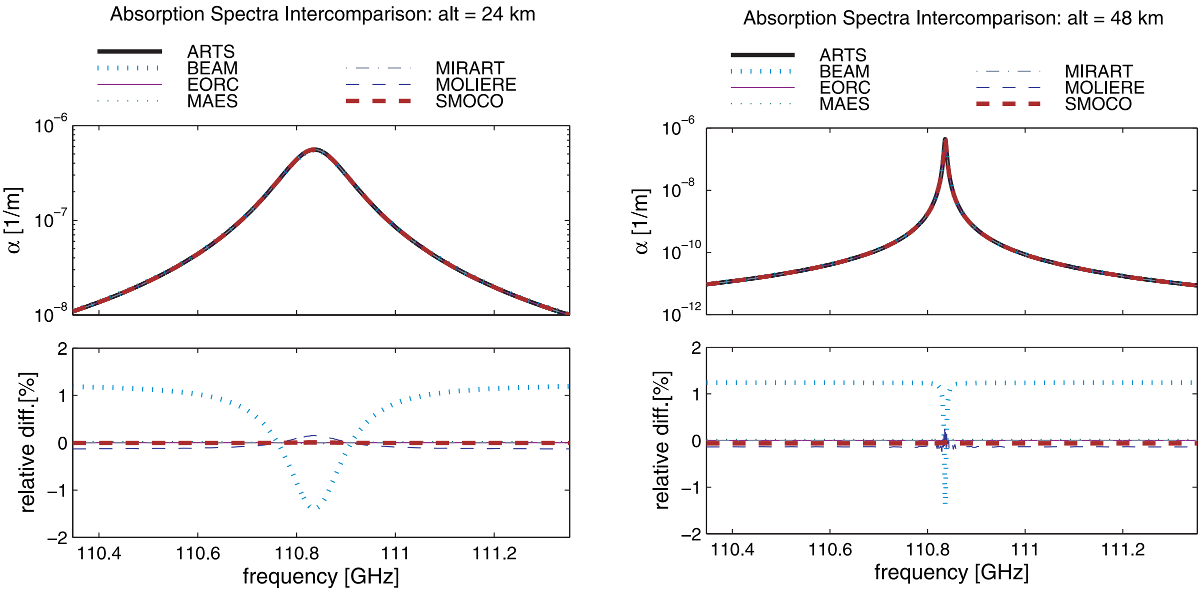

Figure 2. Exercise 0. Top panels show absorption coefficient (O_3 line at 110.83 GHz), at altitudes (left) 24 km and (right) 48 km; temperature 296 K. Bottom panels show relative difference (in percent) of the absorption coefficient with respect to ARTS.

temperature T = 250 K, which corresponds roughly to temperatures in the lower stratosphere, in order to test the implementation of the temperature dependence of the line strength (see equation (5)).

[30] Figure 1 shows the root mean square of the relative deviation of each model from ARTS for the two sets of calculations as a function of altitude. This is defined in the following way: Let $\alpha_{\mathrm{ARTS}}(\nu_i)$ and

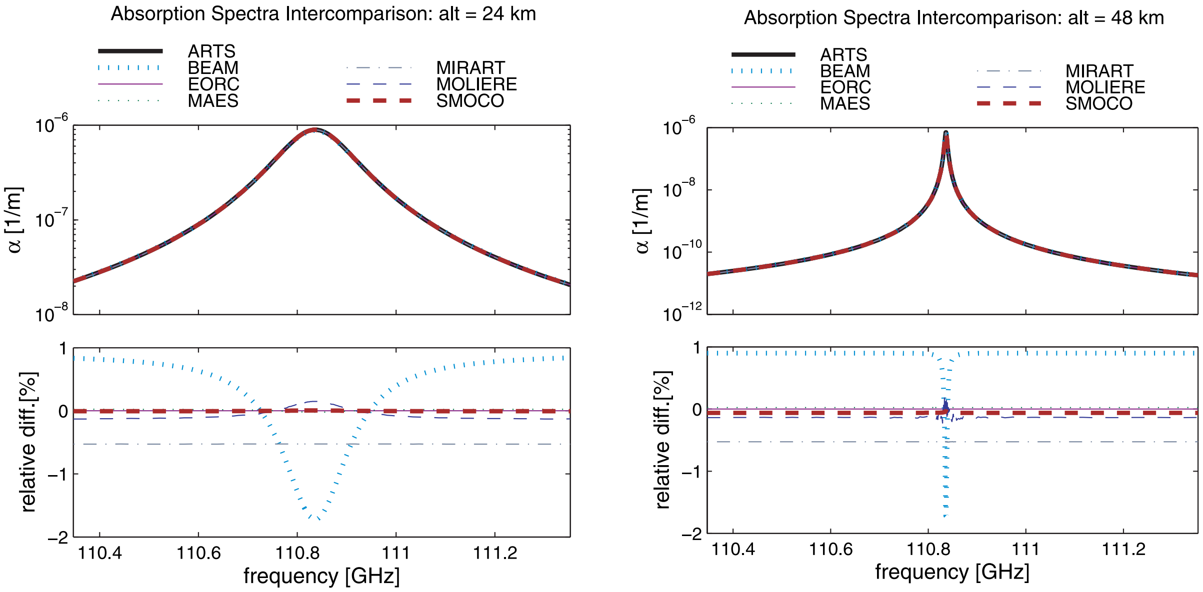

Figure 3. Exercise 0. Top panels show absorption coefficient (O_3 line at 110.83 GHz), at altitudes (left) 24 km and (right) 48 km; temperature 250 K. Bottom panels show relative difference (in percent) of the absorption coefficient with respect to ARTS.

Table 2. Overview of the 12 Frequency Bands Used in Exercises 1A and 2

Band	Frequency, GHz	Species
1	21.73–22.73	H_2O
2	88.00–90.0	(window)
3	110.33–111.33	O_3
4	118.23–119.23	O_2
5	149.00–151.00	(window)
6	182.00–184.00	H_2O
7	353.84–354.84	HCN
8	500.75–502.80	ClO, N_2O
9	543.80–544.80	HNO_3
10	575.76–576.76	CO
11	624.87–626.40	O_3, HCl
12	648.95–649.95	ClO

$\alpha_{\text{other}}(\nu_i)$ be the absorption coefficient at frequency ν_i, calculated by ARTS and by another model, respectively; the frequency grid, $\{\nu_i\}$, has N_ν elements in the given frequency band. The relative deviation of the other model from ARTS is

$$\Delta\alpha_{\text{other}}(\nu_i) = \frac{\alpha_{\text{other}}(\nu_i) - \alpha_{\text{ARTS}}(\nu_i)}{\alpha_{\text{ARTS}}(\nu_i)} \tag{13}$$

Note that here and throughout this study, ARTS was consistently chosen as the reference model just for the sake of convenience. Then the root mean square (RMS) of the relative deviation over the frequency band is

$$\Delta\alpha_{\text{other}}^{\text{RMS}} = \sqrt{\frac{1}{N_\nu}\sum_i [\Delta\alpha_{\text{other}}(\nu_i)]^2} \tag{14}$$

Although the actual vertical coordinate used in all calculations has been pressure, here and for all further plots, we always convert it into altitude which is a more intuitive quantity and therefore more suitable for discussion. The full results (i.e., the calculated absorption coefficient from each model as a function of frequency as well as its relative deviation from ARTS) for some specific altitudes are given in Figures 2 and 3.

5.2. Discussion of Results (Exercise 0)

[31] ARTS, EORC model, SMOCO and MAES are almost identical, regarding both the values of the absorption coefficients and the line shapes; the root mean square of their relative deviation is below 0.1%. The same applies for MIRART at 296 K. The offset by 0.5% (in RMS) of MIRART in the calculation for 250 K (Figure 1 (right panel) and Figure 3) is caused by a different temperature conversion scheme of the line strength. MOLIERE/5 deviates (in RMS) by about 0.2%. In the line wings, it is below ARTS, SMOCO and EORC model with an almost constant offset of about 0.2% for all altitudes, but near the line center, it is above them. It was identified that this is caused by the intercomparison setup: MOLIERE/5 uses a slightly different line width since half widths are specified in MHz/Torr (Verdandi line catalog, cf. Appendix A) whereas HITRAN half widths are provided in cm^{-1}/atm. BEAM deviates by 1% to 1.5% (Figures 1–3); the line wings are higher and the line center is lower than the other models. This was caused by a unit conversion error of 1.3% in the line broadening coefficient that was unfortunately discovered too late for correction.

6. Absorption Coefficient Intercomparison

[32] The intercomparison of the absorption coefficients was made in two steps, checking the correctness of the implementation (exercise 1), and inspecting the spread or variability of the results among the various models when some of the input parameters could be chosen freely, e.g., the line catalog (exercise 2). In exercise 1, line-by-line absorption and continuum absorption were treated separately, thus it is split into exercise 1A and 1B.

6.1. Exercise 1A: Implementation of Line Absorption

[33] The aim of this exercise is to check the correct model implementation for line absorption calculations. Line-by-line calculations of the absorption coefficient were carried out for the 12 frequency bands and 9 species, listed in Table 2. Note that the table lists as "species" for each band only the one or two species that have a major absorption line in that band; the calculations, however were to take into account all lines of those 9 species in all of the 12 given bands. In order to avoid inconsistencies due to variations in input parameters, full spectroscopic data (from HITRAN line catalog), polynomial coefficients for computing the partition function, and the isotopic ratio for each isotope of each target species were provided. The prescribed line shape was the same as in exercise 0 (see equation (12)). As stated above, this line shape behaves like the VVW line shape in the high pressure limit. Therefore KMM also participated in this exercise although it exclusively uses the VVW line shape, keeping in mind that comparison with the other models is then only meaningful for lower altitudes. The frequency step size for the calculations was 10 MHz for the bands with an H_2O line and the window bands, and 5 MHz for all other bands. The atmospheric scenario (pressure, temperature, volume mixing ratio of the gas species) was midlatitude winter, taken from the Air Force Geophysics Laboratory (AFGL) atmospheric data base [*Anderson et al.*, 1986].

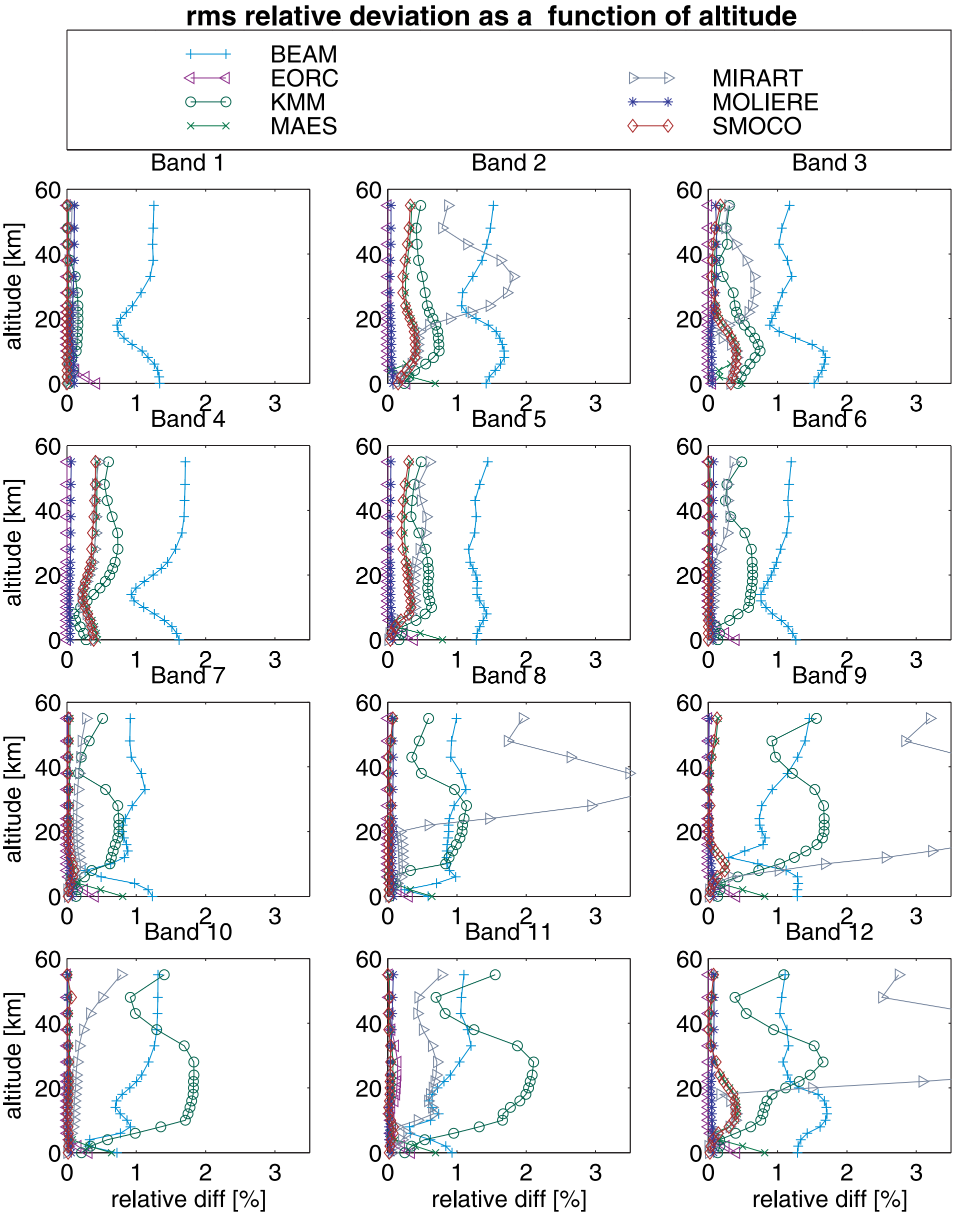

Figure 4. Exercise 1A. Root mean square of the relative deviation from ARTS (in percent) of the participating models as a function of altitude.

The used pressure grid corresponds to altitudes between 0 and 55 km.

6.2. Discussion of Results (Exercise 1A)

[34] Figure 4 shows the root mean square of the relative deviations of the participating models from ARTS, defined as in equation (14), in each of the 12 spectral bands, as a function of altitude. Table 3 shows the maximum relative deviations of all models from ARTS, for all frequency bands, along with the altitudes and frequencies where the maximum deviations for each model occur. In addition, sample plots showing the results for some of the 12 bands at a given altitude are shown in Figures 5–7.

[35] ARTS, SMOCO, MOLIERE/5, and the EORC model are almost identical, their RMS deviation from ARTS is less than 0.5% in frequency band 2 to 5 and less than 0.1% in all other frequency bands (see Figure 4).

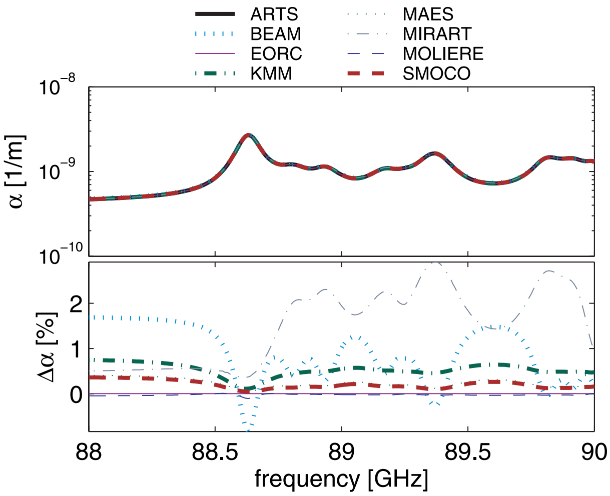

Figure 5. Exercise 1A. (top) Absorption coefficient in window at 89 GHz (band 2) at an altitude of 28 km. (bottom) Relative deviation (in percent) of the different models from ARTS.

The EORC model is closest to ARTS, with a negligible RMS deviation of much less than 0.1% and a maximum deviation of 0.5% (see Table 3). MOLIERE/5 has a RMS deviation from ARTS of less than 0.25%.

[36] BEAM deviates by about 1% (maximum deviation about 1.7%) in all bands. As in exercise 0, the deviations (positive in line wings, slightly negative in line centers, see Figures 5–7) are caused by a unit conversion error of 1.3% in the line broadening.

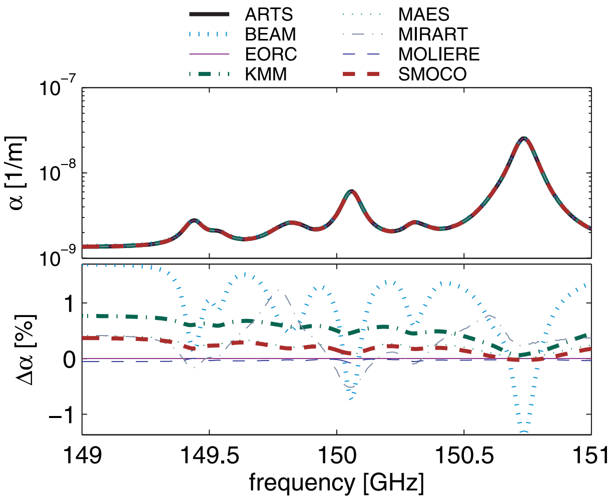

Figure 6. Exercise 1A. (top) Absorption coefficient in window at 150 GHz (band 5) at an altitude of 28 km. (bottom) Relative deviation (in percent) of the different models from ARTS.

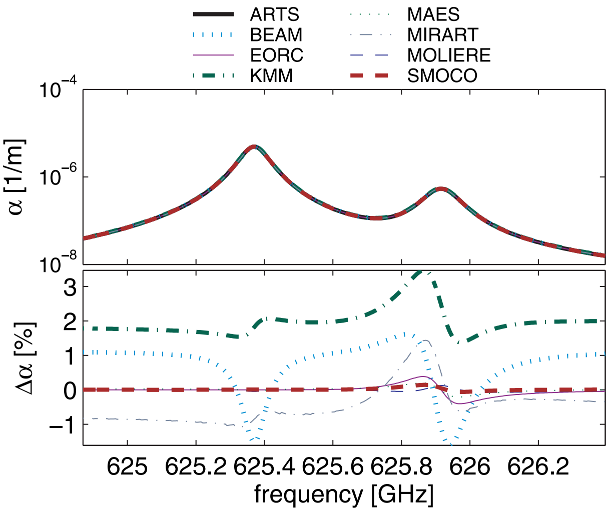

Figure 7. Exercise 1A. (top) Absorption coefficient around O_3 line at 625.37 GHz and HCl line at 625.9 GHz (band 11) at an altitude of 28 km. (bottom) Relative deviation (in percent) of the different models from ARTS.

[37] MAES has mostly a RMS relative deviation from ARTS not greater than 0.1%, only at the lowest altitude it exceeds 0.5%. BEAM has a RMS deviation from ARTS of about 1% (see Figure 4), the maximum deviation does not exceed 2% (see Table 3). The RMS relative deviation of MIRART (Figure 4) exceeds 2% in bands 8, 9, and 12 at altitudes around 30 km. The reason is very likely the temperature conversion scheme of the line strengths: MIRART uses the scheme from the ATMOS software [*Norton and Rinsland*, 1991], whereas ARTS and the other models use the TIPS scheme [*Gamache et al.*, 2000] or other polynomial interpolations of the partition functions. It has been observed that line strengths converted to other temperatures with the ATMOS and the TIPS scheme agree for some molecule species, while there are differences of up to about ±10% for other molecule species. Apparently for the key species of bands 8, 9, and 12, i.e., HNO_3, N_2O, and ClO, the ATMOS and the TIPS schemes differ. Note that the MIRART RMS deviations in bands 8, 9, and 12 are largest at altitudes of about 20 to 30 km, where temperatures are furthest from the reference temperature of 296 K, which is another hint at the temperature conversion's being involved.

[38] KMM and MIRART are close to the other models at the lower altitudes, but near the top of the altitude range they deviate by more than 10% for MIRART and 16% for KMM at 55 km (see Table 3, bands 10 and 11). This is not surprising in the case of KMM, given that it utilizes a VVW line shape function which does not

Table 3. Exercise 1A: Maximum Relative Deviations (%) of the Absorption Coefficient Calculated by the Participating Models From the Absorption Coefficient Calculated by ARTS[a]

	Model						
	BEAM	EORC	KMM	MAES	MIR	MOL	SMOCO
Band 1							
Maximum Deviation, %	−1.373	0.434	0.163	−0.050	0.600	−0.108	−0.015
Altitude, km	4.00	0.00	20.00	0.00	55.00	55.00	33.00
Frequency, GHz	22.23	22.24	22.26	21.73	22.24	22.21	22.05
Band 2							
Maximum Deviation, %	1.722	−0.279	−1.968	−0.692	3.888	0.120	0.409
Altitude, km	10.00	0.00	55.00	0.00	55.00	55.00	12.00
Frequency, GHz	90.00	88.00	89.25	88.00	89.39	88.62	90.00
Band 3							
Maximum Deviation, %	1.697	−0.065	−2.609	−0.489	−2.316	0.150	0.406
Altitude, km	8.00	0.00	55.00	0.00	55.00	38.00	8.00
Frequency, GHz	110.33	110.33	110.84	110.33	110.84	110.84	110.33
Band 4							
Maximum Deviation, %	−1.740	−0.003	−2.559	−0.442	−2.794	0.234	0.417
Altitude, km	4.00	0.00	55.00	0.00	55.00	55.00	55.00
Frequency, GHz	118.75	119.23	118.75	118.77	118.75	118.74	118.77
Band 5							
Maximum Deviation, %	1.712	−0.387	−2.261	−0.794	4.022	0.109	0.406
Altitude, km	33.00	0.00	55.00	0.00	55.00	55.00	55.00
Frequency, GHz	149.00	151.00	150.35	151.00	150.64	150.30	149.00
Band 6							
Maximum Deviation, %	−1.634	0.435	−4.210	−0.152	−2.537	−0.126	−0.054
Altitude, km	43.00	0.00	55.00	0.00	55.00	55.00	48.00
Frequency, GHz	182.18	183.31	182.18	182.00	182.18	183.96	182.38
Band 7							
Maximum Deviation, %	−1.694	−0.405	4.885	−0.806	1.923	−0.077	0.112
Altitude, km	43.00	0.00	55.00	0.00	55.00	0.00	8.00
Frequency, GHz	354.50	353.84	354.50	353.84	354.51	354.82	353.84
Band 8							
Maximum Deviation, %	−1.767	−0.327	−6.021	−0.706	8.022	−0.119	0.171
Altitude, km	43.00	0.00	55.00	0.00	55.00	43.00	55.00
Frequency, GHz	502.30	500.75	502.29	500.75	502.30	502.30	502.80
Band 9							
Maximum Deviation, %	1.615	−0.406	7.893	−0.814	9.303	−0.079	0.268
Altitude, km	55.00	0.00	55.00	0.00	55.00	0.00	55.00
Frequency, GHz	543.80	543.80	544.37	543.80	544.42	544.79	543.80
Band 10							
Maximum Deviation, %	1.356	−0.319	−15.689	−0.654	8.780	−0.063	0.078
Altitude, km	33.00	0.00	55.00	0.00	55.00	0.00	48.00
Frequency, GHz	575.76	575.76	576.26	575.76	576.27	575.76	575.76
Band 11							
Maximum Deviation, %	1.813	−0.402	15.829	−0.709	6.480	−0.135	0.145
Altitude, km	33.00	28.00	55.00	0.00	55.00	55.00	28.00
Frequency, GHz	625.86	625.97	625.37	624.87	625.92	626.03	625.87
Band 12							
Maximum Deviation, %	1.715	−0.405	−14.005	−0.813	−11.260	0.096	0.395
Altitude, km	12.00	0.00	55.00	0.00	55.00	28.00	12.00
Frequency, GHz	649.95	649.95	649.45	648.95	649.45	649.45	649.95

[a] Listed are also the altitude and the frequency where the maximum deviation of each model occurs. MIR = MIRART, MOL = MOLIERE/5.

Table 4. Specific Input of Those Parameters That Could Be Chosen Freely in Exercise 2

		Line Shape[b]			
Model	Catalog[a]	Low	High	γ_L/γ_D	Continual Absorption[c]
ARTS	H, o.[d]	Vo, o.[d]		–	PWR, MPM93[d]
BEAM	B	Vo		–	MPM93 (H_2O, dry air)
EORC	J	VVW		–	MPM93
KMM	H	VVW		–	MPM89
MAES	J (H)	Lo	Vo[e]	20	MPM93
MOLIERE/5	V[f]	VVW	Vo	40	MPM93 (H_2O, dry air)
SMOCO	J (H)	Vo		–	MPM93

[a] The spectral line catalog used. "J" is for JPL line catalog [*Pickett et al.*, 1998], "H" is for HITRAN line catalog [*Rothman et al.*, 1998], "B" is for BEAMCAT catalog (cf. Appendix A), "V" is for Verdandi catalog (cf. Appendix A), and "J(H)" is the JPL catalog with pressure broadening parameters from the HITRAN catalog.

[b] The line shape function used; some models use two different ones, one for low, one for high altitude (columns low and high, respectively). The switch from low to high altitude takes place where the ratio γ_L/γ_D falls below a critical value, given in the column "γ_L/γ_D." "Vo" is Voigt (cf. equation (9)), "VVW" is Van Vleck–Weisskopf (cf. equation (8)), and "Lo" is Lorentz (cf. equation (7)).

[c] The model used for continuum absorption: MPM89,93 [*Liebe*, 1989; *Liebe et al.*, 1993] and PWR model [*Rosenkranz*, 1993, 1998].

[d] O_3, ClO, HCN, CO, HCl, HNO_3, and N_2O are from HITRAN, using hybrid line shape; H_2O and O_2 continuum and lines are from PWR [*Rosenkranz*, 1993, 1998]; and N_2 continuum is from MPM93.

[e] Simple Gaussian function used at higher altitude where $\gamma_L/\gamma_D < 100$.

[f] Selection of lines: all absorption lines between 0 and 700 GHz whose line center intensity exceeds 10 mK (with respect to 20, 35, or 50 km limb view).

account for the increased role of the Doppler broadening at greater heights. This line shape contributes also to an expected distortion of the line profile, overestimating it to the left of the line center and underestimating to the right. In both the window bands (i.e., band 2 and 5, Figures 5 and 6) the line intensities are a bit overestimated by KMM. The peculiar deviations of MIRART in band 5 at 28 km (Figure 6), i.e., peaks at about 149.8 and 150.6 GHz, are apparently another consequence of the above mentioned different temperature conversion scheme of line strength MIRART uses: At the frequencies where these peaks occur, there are minor lines of HNO_3, for which the temperature conversion schemes seem to disagree. Note that the lines at 149.8 and 150.6 GHz themselves are hidden in the wing of stronger lines.

[39] In band 11 (Figure 7), some probably overlapping artifacts in the right wing range cause an even higher deviation than the deviation produced by the different line shape. In addition, KMM shows a slight positive offset (about 1% at 30 km, see Figures 5–7). For the HCl line at 625.9 GHz (in band 11), the pressure shift has not been considered by BEAM, the EORC model, KMM and MIRART (see Figure 7, the asymmetric feature, a peak followed by a depression).

6.3. Exercise 1B: Implementation of Continuum Absorption

[40] The aim of this exercise is to check the implementation of the millimeter-wave propagation model, MPM93 [*Liebe et al.*, 1993], for water vapor continuum and line absorption in the frequency range from 1 GHz to 1 THz. The oxygen and nitrogen absorption part of this model is excluded from the calculation.

6.4. Discussion of Results (Exercise 1B)

[41] The models which participated in this exercise were ARTS, BEAM, EORC model, MAES, MOLIERE/5 and SMOCO (KMM has MPM89, not MPM93).

[42] The implementation check is found to give good agreement to within 1% for the continuum part of MPM93. However, a few inaccuracies in the MPM93 line list caused large discrepancies because these inaccuracies were corrected to varying extent in the different models. The problems/inaccuracies of MPM93 mentioned are as follows.

[43] 1. Missing isotopic ratios for two lines near 550 GHz, namely at 547.67 GHz, $H_2^{18}O$ (abundance: 0.00199983) and 552.02 GHz, $H_2^{17}O$ (abundance: 0.00037200); see also *Kuhn* [2004].

[44] 2. In MPM93, a line at 645.866 GHz has been added while actually there should be two lines at 645.766 GHz and 645.905 GHz; see *Bauer et al.*, [1989] and *Kuhn* [2004] for spectroscopic parameters.

[45] 3. An inaccuracy of the conversion formula (provided with MPM85 [*Liebe*, 1985]) from HITRAN format to MPM format. It contains an approximation for large lower state energies that may not be applicable for all lines.

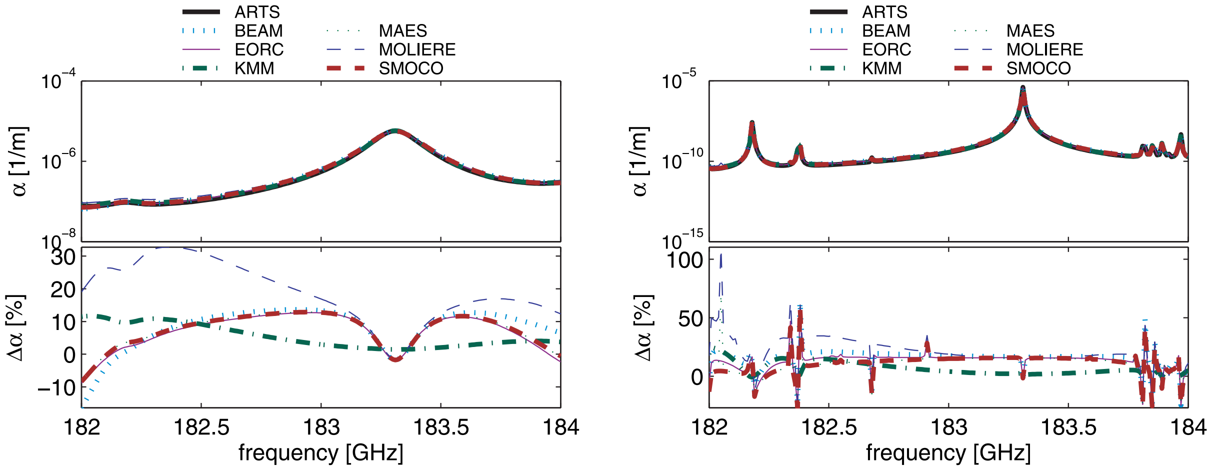

Figure 8. Exercise 2. Top panels show absorption coefficient around H_2O line at 183.31 GHz (band 6), (left) altitudes 24 km and (right) 48 km. Bottom panels show relative deviation of the different models from ARTS (in percent). Differences are apparently caused by differences in line shape and in continuum absorption modeling.

6.5. Exercise 2: Model Differences

[46] The aim of this exercise is to investigate the spread or variability among the models in absorption calculations when the model-specific standard input is used: Absorption coefficients were computed for specified atmospheric conditions (midlatitude winter, as above, according to *Anderson et al.* [1986]) and frequencies, but the remaining parameters, i.e., line shape, line catalog, line selection, and continuum absorption were to be chosen by the participants. The calculations were carried out for a set of target species which have a signature in the given frequency range. A standard continuum absorption used by each model was added to the line absorption. The spread of the results among the models gives a rough idea about the discrepancy between models under realistic conditions. The calculations were performed for the same 12 bands as in exercise 1A (see Table 2). The specific input parameters chosen for each model are listed in Table 4.

[47] Note that the oxygen absorption model of Rosenkranz was recently updated compared to the 1993

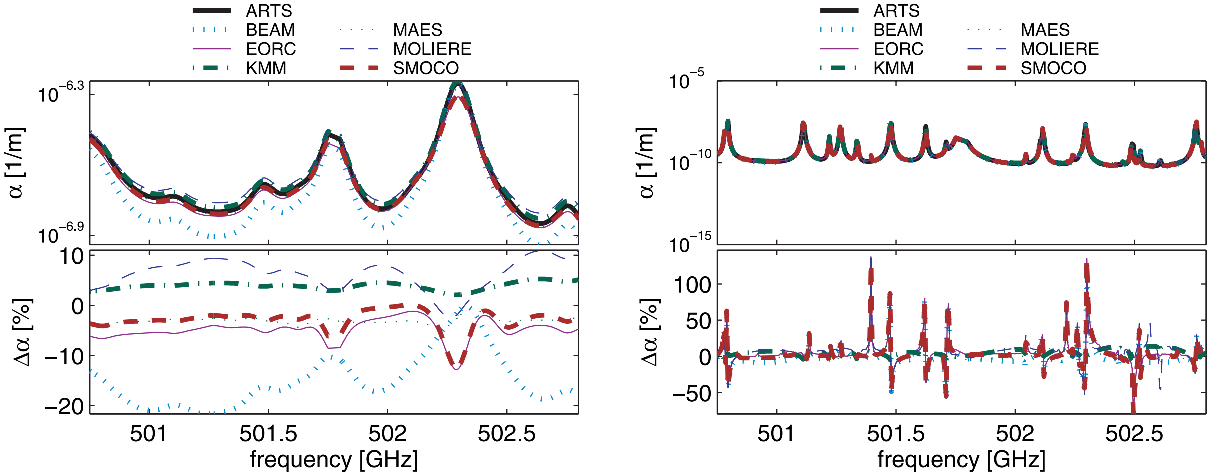

Figure 9. Exercise 2. Top panels show absorption coefficient in the spectral range including ClO line at 501 GHz and N_2O line at 502 GHz (band 8), altitudes (left) 24 km and (right) 48 km. Bottom panels show relative deviation of the different models from ARTS (in percent). Differences are apparently caused by differences in line shape and in continuum absorption modeling.

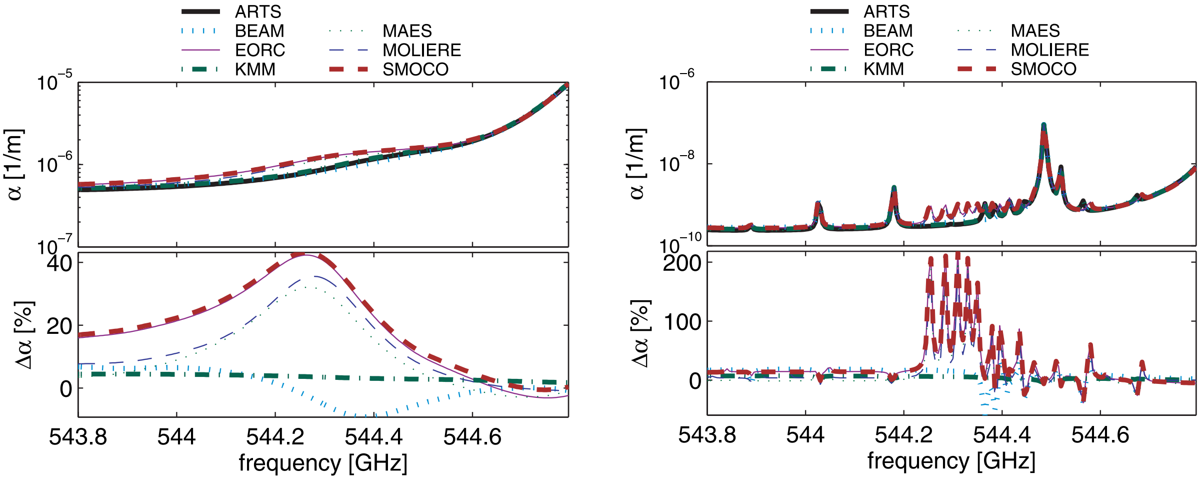

Figure 10. Exercise 2. Top panels show absorption coefficient around HNO_3 line cluster at 544 GHz (band 9), altitudes (left) 24 km and (right) 48 km. Bottom panels show relative deviation of the different models from ARTS (in percent). Apparently, EORC model, MAES, MOLIERE, and SMOCO considered some additional lines between about 544.2 and 544.35 GHz.

version (see ftp://mesa.mit.edu/phil/lbl_rt). The update affects the 118 GHz line broadening (updated as described in the work of *Schwartz* [1997]) and the submillimeter line intensities (updated using HITRAN96 line intensities). This new version was used for the ARTS calculations.

6.6. Discussion of Results (Exercise 2)

[48] In general, near line centers, all models yield absorption coefficients within about 10% of each other. However, in the line wings where the absorption coefficient is very low, the different line shapes and continuum absorption models chosen by the different models result in very high relative differences because of the very low absolute values (see, e.g., Figures 8 and 9). The same applies for lines taken into account by one model but ignored by another (see Figure 10), and for discrepancies of line center frequencies (see Figure 11). Note that differences in the continuum models are usually not critical for applications such as trace gas retrievals since

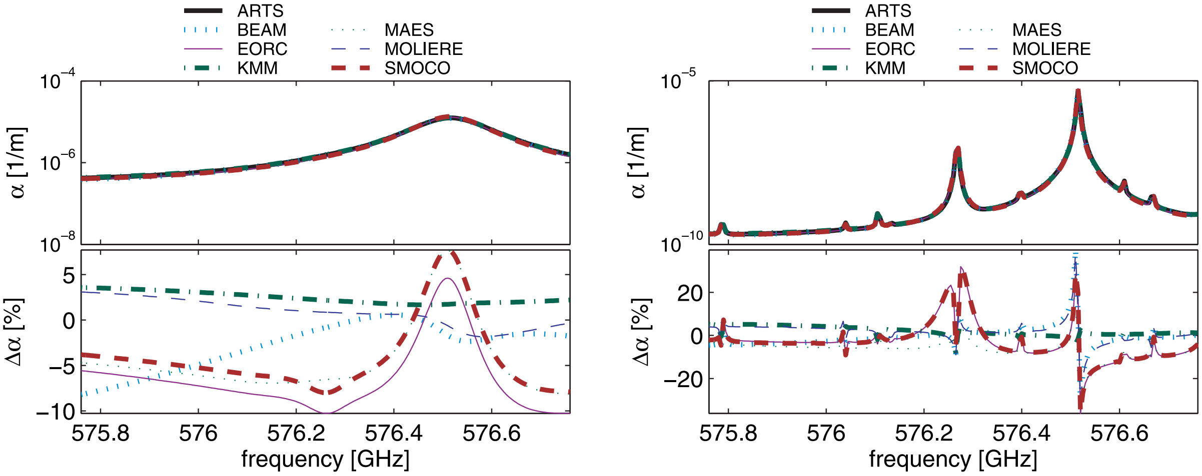

Figure 11. Exercise 2. Top panels show absorption coefficient around CO line at 576 GHz (band 10), altitudes (left) 24 km and (right) 48 km. Bottom panels show relative deviation of the different models from ARTS (in percent). Apparently, there are discrepancies in the center frequency of the line near 576.6 GHz.

Table 5. AMSU-B Channel Characteristics

Channel	Center Frequency, GHz	Bandwidth of Passbands, MHz
16	89.0 ± 0.9	1000
17	150.0 ± 0.9	1000
18	183.31 ± 0.9	500
19	183.31 ± 3.0	1000
20	183.31 ± 7.0	2000

continuum absorption can be retrieved from the measurement (see also section 8.6). In contrast, discrepancies in the lines, such as missing or additional lines (Figure 10), errors in line center frequencies (Figure 11) or in line broadening parameters may lead to large systematic retrieval errors.

7. Radiative Transfer Intercomparison

[49] The radiative transfer intercomparison was carried out for checking the implementation (exercise 3) and inspecting the variability (spread) among the models when input parameters were free (exercise 4). For each exercise the calculations were performed for three different configurations that correspond to three typical sensor types in atmospheric sounding: (1) a down-looking sensor like Advanced Microwave Sounding Unit-B (AMSU-B) [*Vangasse et al.*, 1995], (2) a limb-looking sensor like Millimeter-wave Acquisitions for Stratosphere/Troposphere Exchange Research (MASTER) [*Reburn et al.*, 2000], and (3) an up-looking sensor like RAM [*Langer et al.*, 1996]. For each configuration and exercise, specific input was provided.

[50] In order to simulate the effect of the sensor, the characteristics of (1) the antenna, (2) the radiometer (particularly the mixer and receiver), and (3) the spectrometer were specified: The antenna pattern, the sideband ratio, and the spectrometer's channel response functions.

[51] The characteristics of the down-looking sensor were chosen to simulate AMSU-B: The AMSU-B channel characteristics are given in Table 5. The sensor was assumed to have a perfect antenna (i.e., the antenna pattern is a delta function), and to be a perfect double sideband receiver (both sidebands have equal weight). The spectrometer was assumed to have a perfect rectangular response function with a width equal to the bandwidth of the passband corresponding to each channel. The viewing angle, by which we shall always mean the zenith angle of the sensor's pointing direction, ranges from 130° to 180° (nadir-looking), in steps of 1°. The platform altitude was assumed to be 833 km, the ground temperature 271 K and the ground surface emissivity 1.0.

[52] The characteristics of the limb-looking sensor were chosen as follows: The simulated antenna is

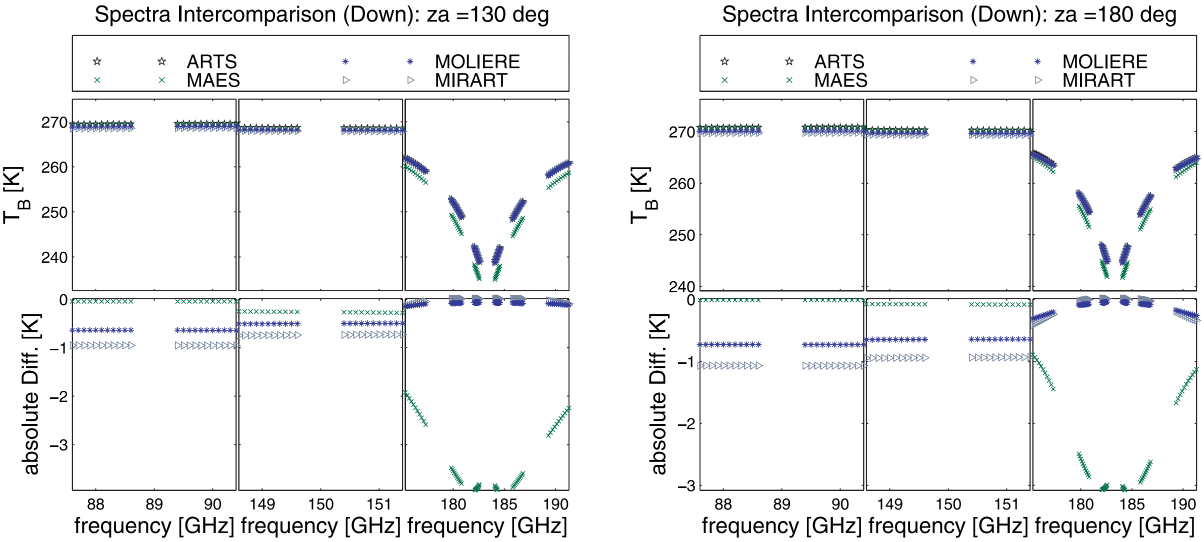

Figure 12. Exercise 3, down-looking geometry. Top panels show monochromatic spectra calculated by ARTS, MAES, MIRART, and MOLIERE/5 and bottom panels show the absolute deviation from ARTS. The plots are for the extreme viewing angles (left) 130° and (right) 180°, i.e., nadir. Each plot is subdivided into three frequency ranges: The leftmost contains the two sidebands of AMSU channel 16, and the middle one contains the two sidebands of AMSU channel 17. The rightmost one contains the two sidebands of each of the three AMSU channels centered around the H_2O line at 183.31 GHz (cf. Table 5): channel 18 (innermost pair of curve segments), channel 19, and channel 20 (outermost pair).

Table 6. Exercise 3, Down-Looking Geometry[a]

Zenith Angle, deg	Model MAE	 MIR	 MOL
Channel 16			
130	−0.04	−0.95	−0.64
140	−0.02	−1.01	−0.69
150	−0.02	−1.05	−0.71
160	−0.01	−1.06	−0.72
180	−0.01	−1.07	−0.73
Channel 17			
130	−0.26	−0.74	−0.50
140	−0.15	−0.84	−0.58
150	−0.11	−0.89	−0.61
160	−0.09	−0.92	−0.63
180	−0.08	−0.94	−0.64
Channel 18			
130	−3.92	−0.58	−0.07
140	−3.54	−0.56	−0.05
150	−3.30	−0.57	−0.04
160	−3.16	−0.55	−0.04
180	−3.06	−0.54	−0.05
Channel 19			
130	−3.70	0.02	−0.08
140	−3.29	0.01	−0.07
150	−3.03	−0.00	−0.07
160	−2.86	0.00	−0.08
180	−2.74	−0.00	−0.08
Channel 20			
130	−2.39	−0.06	−0.11
140	−1.86	−0.15	−0.16
150	−1.56	−0.22	−0.19
160	−1.38	−0.25	−0.22
180	−1.26	−0.29	−0.24

[a] Deviation of brightness temperatures (in K) as would be recorded by sensor (AMSU-B), calculated by MAES, MIRART, and MOLIERE/5 from those calculated by ARTS, for the 5 channels of AMSU-B and various viewing angles (180° = nadir).

assumed to have a Gaussian pattern, with a width of the main beam (full width at half maximum (FWHM) of the Gaussian function) of 0.07°. A perfect single sideband sensor was assumed, and a spectrometer where all 350 channels have the same Gaussian response function with a FWHM of 20 MHz, covering a frequency range from 498.5–506.25 GHz. The assumed platform altitude was 800 km, the tangent altitude range is 60–10 km in steps of 2 km. Surface temperature of the ground was assumed to be 272 K, ground surface emissivity 1.0.

[53] The characteristics of the up-looking sensor were chosen as follows: The sensor is assumed to have a perfect antenna (pencil beam), and be a perfect single sideband receiver. All 2400 channels of the spectrometer are assumed to have a Gaussian response function with a FWHM of 0.5 MHz, covering the frequency band from 141.58–142.78 GHz (O_3 absorption line). Viewing (i.e., zenith) angles range from 0° (zenith) to 80°, in steps of 4°. The platform altitude was assumed to be 10 km (as for an airborne up-looking instrument).

7.1. Exercise 3: Radiative Transfer Implementation

[54] The aim of this exercise is to investigate the differences between the models due solely to the numerical solution of the radiative transfer equation (1). The three geometries, limb, up, and down looking, were considered. For each geometry of concern a standard set of absorption coefficient spectra was used as input, calculated by using the HITRAN database, H_2O and N_2 continuum model by *Liebe* [1989], O_2 continuum model by *Rosenkranz* [1993]. The atmospheric scenario, again, was midlatitude winter [*Anderson et al.*, 1986].

[55] For given specifications, the precalculated absorption spectra were used to derive the spectra of pencil beam monochromatic brightness temperature ("monochromatic (pencil beam) spectra") for a set of viewing directions specific to each geometry, and the spectra as would be recorded by the sensor with given characteristics (antenna pattern, spectrometer response, sideband ratio). Two sets of calculations were performed, one with the input absorption coefficients given on a coarse grid (45 pressure grid points corresponding to altitudes between 0 and 95 km, spaced about 1 to 5 km apart), the other with the input absorption coefficients given on a fine grid (264 pressure grid points corresponding to altitudes between 0 and 95 km, spaced about 160 to 750 m apart). Refraction of the radiation by the atmosphere was not considered.

7.2. Discussion of Results (Exercise 3)

7.2.1. Down-Looking (AMSU-B Type)

[56] Participating models: ARTS, MAES, MOLIERE/5, MIRART. Monochromatic pencil-beam spectra for the extreme viewing angles of 130° and 180° (nadir) are shown in Figure 12, and the "spectra" as would be recorded by the sensor AMSU-B (here just an average over each band), for various viewing angles, are shown in Table 6. In the two window channels (16 and 17), all models are well within less than 1 K of each other. In the three water vapor channels (18 to 20), they are even closer, except for MAES which deviates by up to 4 K. The cause is very likely to be in the radiative transfer calculations, for MAES was very close to ARTS in the line shape implementation test (exercise 0) and the absorption calculation test (exercise 1 and 2). Note that all results shown here are from calculations on the fine grid. The spectra calculated on the coarse grid were not significantly different.

7.2.2. Limb-Looking (Master Type)

[57] Participating models in this exercise are ARTS, EORC, MAES, MIRART, MOLIERE/5 and SMOCO.

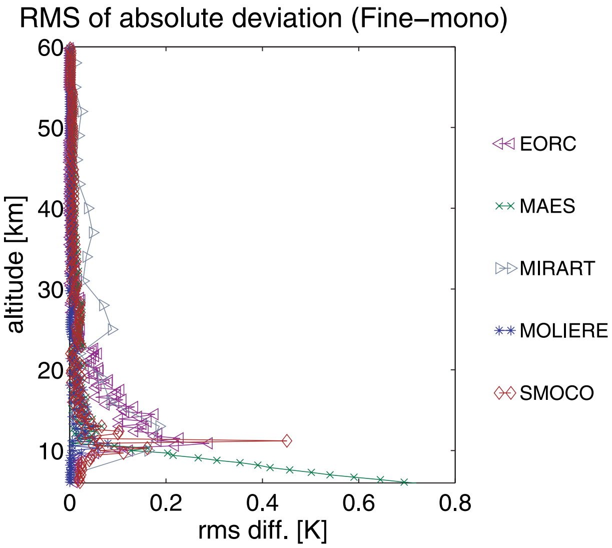

Figure 13. Exercise 3, limb-looking geometry. Root mean square of the absolute deviation of the monochromatic pencil beam spectra with respect to ARTS as a function of tangent altitude.

7.2.2.1. Monochromatic Pencil-Beam Spectra

[58] Figure 13 displays the root mean square of the absolute deviation from ARTS calculations as a function of tangent altitude. Figure 14 shows the brightness temperature, and the absolute deviation from ARTS for two particular tangent altitudes (16 km and 46 km).

[59] ARTS and MOLIERE/5 almost exactly match (difference less than 0.02 K). SMOCO results are also close to ARTS results. The only notable deviation appears at only one altitude around 11 km; the deviation from ARTS at other altitudes is less than 0.08 K. The EORC model and MIRART deviate by at most 0.2 K (at 11 km), but less than 0.01 K (EORC model) and 0.1 K (MIRART) at altitudes above 25 km. MAES shows a noteworthy deviation of about 0.7 K only at the lowest altitudes; otherwise, it is within 0.1 K of ARTS. Note that in the used atmospheric scenario (midlatitude winter from AFGL data base, see section 6.1), the sharp tropopause is at about 10.5 km, which explains the large deviations at 11 km.

7.2.2.2. Spectra As Would Be Recorded by the Sensor

[60] Figure 15 displays the root mean square of the absolute deviation from ARTS as a function of tangent altitude. Figure 16 shows the brightness temperature and the absolute difference for two tangent altitudes (14 km and 46 km). The agreement between all models except MIRART at low altitudes is rather good, with differences below 0.1 K, up to tangent altitudes of 30 km. Above 30 km the deviation of all the models from ARTS and EORC model is increasing with increasing altitude (Figure 15), MAES, MOLIERE/5, and SMOCO reaching a value of about 0.5 K at altitudes of 50 km. MIRART deviates slightly more, up to 1.3 K at 40 km,

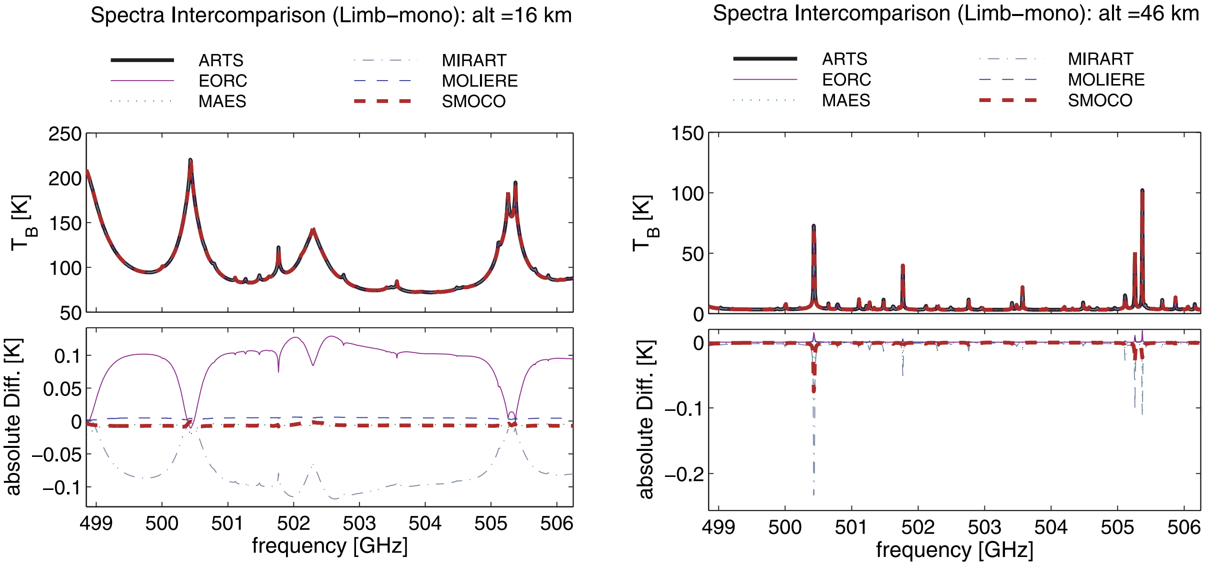

Figure 14. Exercise 3, limb-looking geometry. Top panels show monochromatic spectra, and the bottoms panels show absolute deviation with respect to ARTS for all the participating models. The results are displayed for tangent altitudes of (left) 16 km and (right) 46 km.

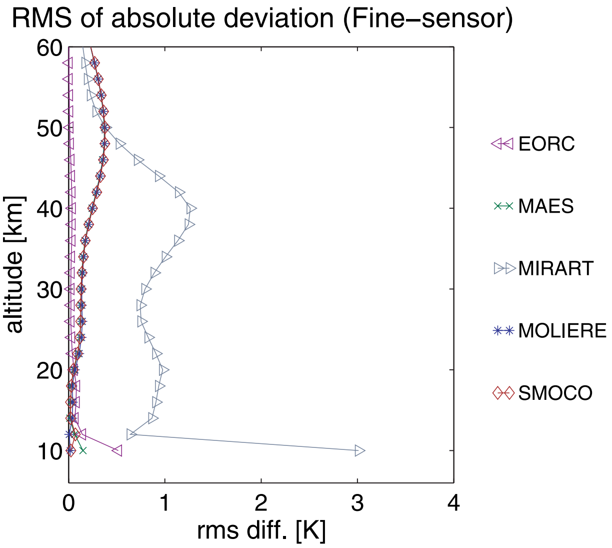

Figure 15. Exercise 3, limb-looking geometry. Root mean square of the absolute deviation of spectra as would be recorded by the sensor, with respect to ARTS, as a function of tangent altitude.

and 3 K at the lowest altitudes. Investigating the deviation as a function of frequency, we found a maximum of 15 K for MIRART at only a few grid points resulting from the use of a different frequency grid internally in MIRART. The deviation of MIRART at 14 km (Figure 16, left plot) is probably caused by the different numerical quadrature scheme MIRART uses (see Appendix A) for calculating the radiative transfer, i.e., the Schwarzschild equation; similar deviations have been found between results calculated with just one model, MIRART, but using different quadrature schemes.

[61] Apart from that, MIRART matches well as is seen from the root mean square deviation mentioned above. In this sense the root mean square deviation is a better measure for the overall agreement of two models than the maximum deviation that is possibly only found at a few frequency grid points.

7.2.3. Up-Looking (RAM Type)

[62] The models participating in this exercise are ARTS, KMM, MAES, MIRART and MOLIERE/5. Figure 17 shows the brightness temperature and the absolute difference with respect to ARTS for two particular viewing angles (0° = zenith, 80°); Figure 18 shows the root mean square of the absolute deviation of the monochromatic pencil-beam spectra from ARTS as a function of viewing angle, i.e., zenith angle, and Figure 19 shows the root mean square of the absolute deviation of the spectra as would be recorded by the sensor (RAM), as a function of viewing angle.

[63] All the participating models agree very well for all viewing angles. The differences from the reference model ARTS are very small and mostly at the line centers. As a general feature, the deviation from ARTS increases with increasing viewing angle (or, in other

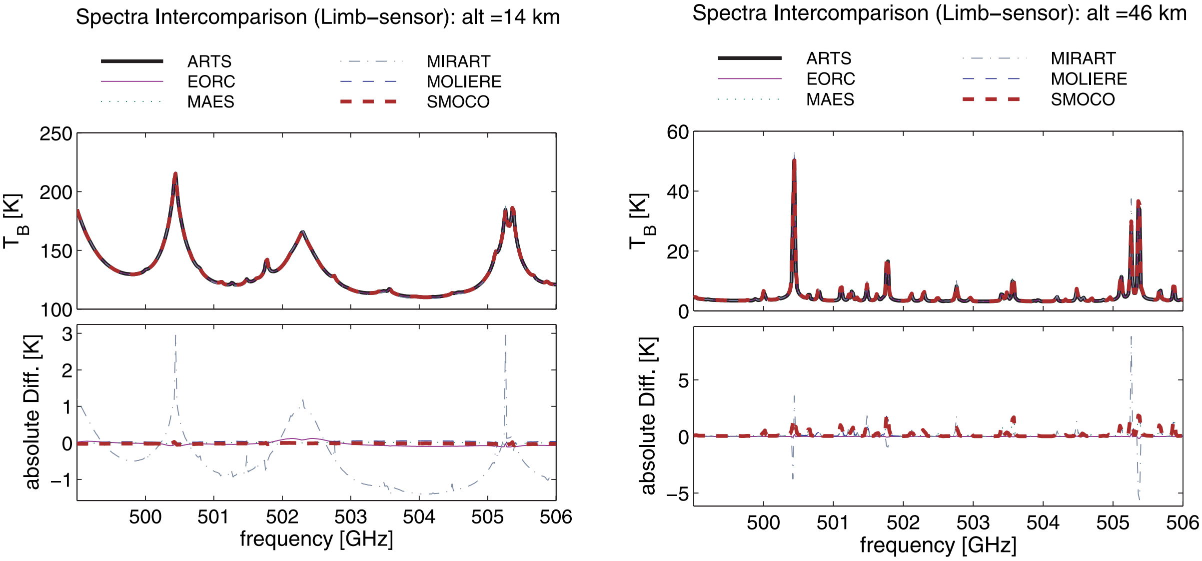

Figure 16. Exercise 3, limb-looking geometry. Top panels show spectra as would be recorded by sensor, and bottom panels show absolute deviation with respect to ARTS for all the participating models. Tangent altitudes (left) 14 km and (right) 46 km.

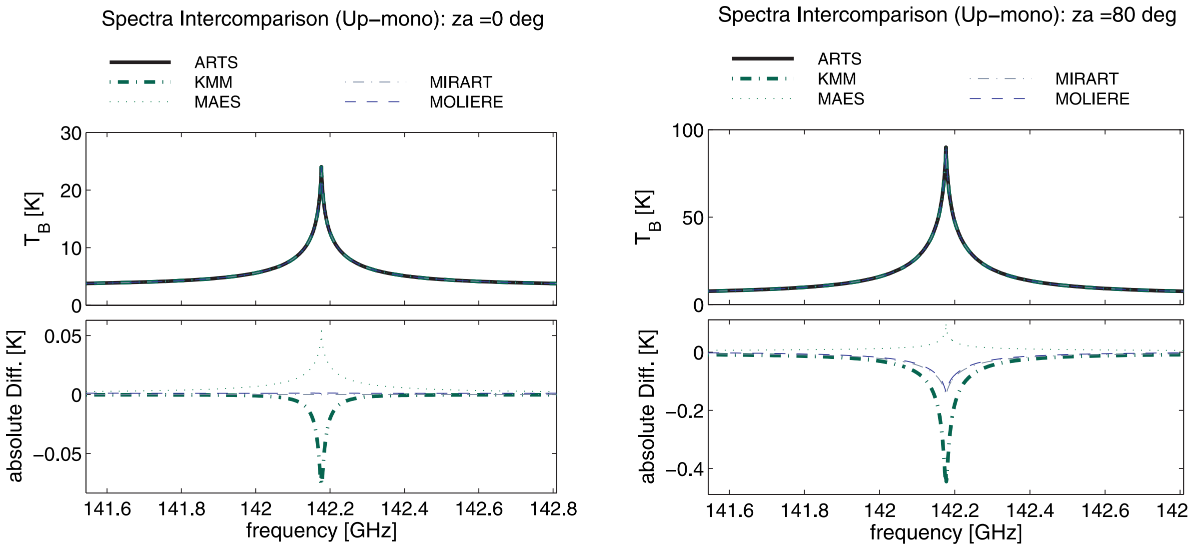

Figure 17. Exercise 3, up-looking geometry. Top panels show monochromatic spectra calculated by ARTS, KMM, MAES, MIRART, and MOLIERE/5, and the bottom panels show absolute deviation from ARTS for all the participating models. Viewing angles (left) 0°, i.e., zenith-looking, and (right) 80°.

words, ARTS deviates from the other models with increasing viewing angle). However, the deviation is generally below 0.2 K. The simulations also show that maximum difference between the models occurs close to the line center and then diminishes toward the line wings.

7.3. Exercise 4: Model Differences

[64] The aim of this exercise is to inspect the variability (spread) among the models when they use their standard inputs: The radiative transfer calculations were carried out for given atmospheric conditions corresponding to the midlatitude winter [*Anderson et al.*, 1986], and for given sensor characteristics, but all other parameters (spectroscopic data, line shape, line selection, continuum absorption model) were not fixed. As in exercise 2, the spread of the results among the models gives a rough idea about the discrepancy between models under realistic conditions.

[65] The comparison was carried out for all three configurations mentioned above (exercise 3), i.e., AMSU-B type (down-looking), MASTER type (limb-looking), and RAM type (up-looking) with the same sensor characteristics as in exercise 3. For a given set of viewing directions, the spectra as they would be recorded by the sensors were calculated. In contrast to exercise 3, refraction was to be taken into account.

[66] The calculations with BEAM, EORC, KMM, and SMOCO used the same setup as in exercise 2 (see section 6.5, Table 4). MAES used the same setup except for a different threshold altitude for the switch from Lorentz to Voigt line shape: The threshold altitude was set to the altitude where the pressure broadening width γ_L becomes twice the Doppler broadening width γ_D. The Lorentz line shape function is used at altitudes below the threshold.

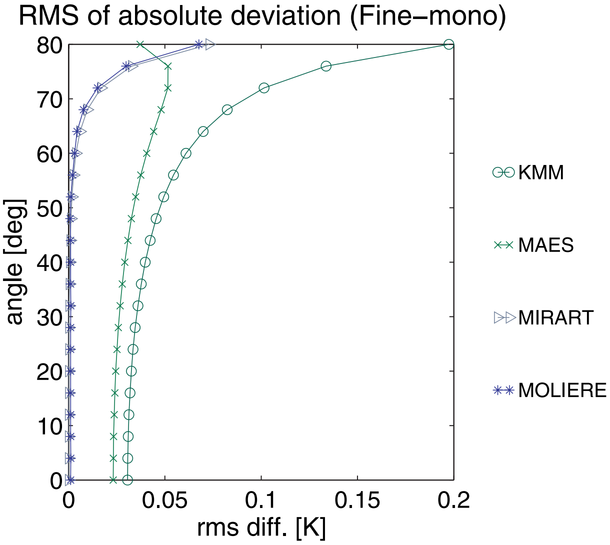

Figure 18. Exercise 3, up-looking geometry. Root mean square of absolute deviation of monochromatic spectra with respect to ARTS, as a function of viewing angle.

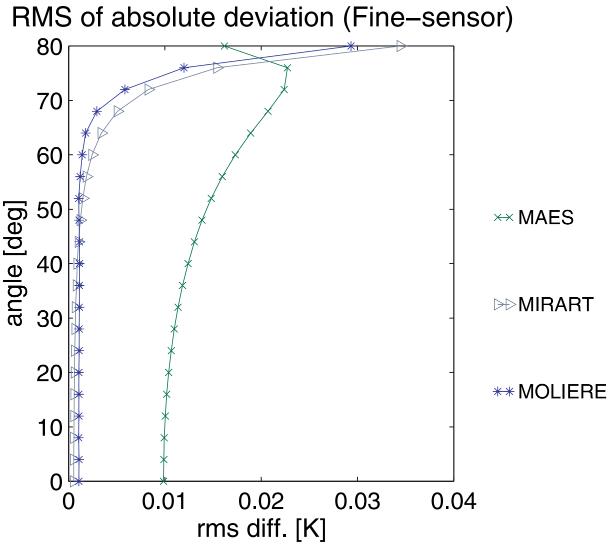

Figure 19. Exercise 3, up-looking geometry. Root mean square of absolute deviation of spectra as would be recorded by the sensor, with respect to ARTS, as a function of viewing angle.

[67] ARTS used the same setup as in exercise 2 except for the continuum model for N_2 for up- and down-looking geometry: Here, the model by Rosenkranz [*Janssen 1993*, chapter 2] was used.

[68] The setup for MIRART: HITRAN line catalog; Voigt line shape function with a prefactor of $(\nu/\nu_0)^2$ and a line-wing cutoff at 10 cm^{-1}. For H_2O lines: a cutoff at 25 cm^{-1} and subtraction of $F_{\mathrm{Voigt}}(25\ \mathrm{cm}^{-1})$) was used, appropriate for the CKD continuum absorption model (cf. Appendix A).

[69] The setup of MOLIERE/5 is the same as in exercise 2, except for different selection criteria of the absorption lines included in the calculations: For the limb-looking (MASTER-E type) configuration, all lines between 477 and 527 GHz having a minimum contribution of 10 mK to the target interval (496.9 to 507.1 GHz) were selected; cosmic background was taken into account. For the down-looking (AMSU-B type) configuration (three separate frequency ranges, see Table 5), lines between 69 and 89 GHz, between 130 and 150 GHz, and between 163.31 and 183.31 GHz having 10 mK sensitivity with respect to target intervals (87.6 to 88.6 GHz, 148.6 to 149.66 GHz, and 175.31 to 182.66 GHz, respectively, and corresponding image bands) were selected; the ground was treated as a blackbody at the temperature of the lowest atmospheric layer. For the up-looking (RAM type) configuration, lines between 122.175 and 162.175 GHz having 10 mK sensitivity with respect to target interval (141.57 to 142.78 GHz) and the corresponding image band were selected; cosmic background was taken into account.

7.4. Discussion of Results (Exercise 4)

7.4.1. Down-Looking

[70] Data from ARTS, MAES, MIRART and MOLIERE/5 are available in this exercise. The absolute deviation of the results from ARTS is shown in Table 7. The highest deviations of about 4 K occur at channel 19 and 20 for MAES, and at channel 16 for MOLIERE/5. Deviations are the larger, the more off-nadir the viewing angle (i.e., the longer the path through the atmosphere). They are probably caused by differences in the continuum absorption modeling.

7.4.2. Limb-Looking

[71] The models which participated in this exercise are ARTS, EORC model, MAES, MIRART, MOLIERE/5 and SMOCO. The RMS deviations of the different models from ARTS are shown in Figure 20. The results for tangent altitudes of 12 km and 52 km are shown in Figure 21.

[72] At low altitudes the smallest deviations are found in the line centers and the largest deviations are found in the wings. This can be mainly explained by the different continuum absorption models which have been used to calculate the absorption coefficients. Absolute deviations are around 20 K. MOLIERE/5 is 20 K higher than ARTS, MIRART is 20 K lower. EORC model and MAES and SMOCO are very similar.

Table 7. Exercise 4, Down-Looking Geometry[a]

Zenith Angle, deg	Model		
	MAE	MIR	MOL
	Channel 16		
130	0.80	−5.76	−4.72
180	0.89	−3.31	−2.51
	Channel 17		
130	−0.29	−3.81	−2.65
180	0.37	−2.32	−1.39
	Channel 18		
130	−3.71	−0.20	−0.42
180	−2.71	−0.04	−0.13
	Channel 19		
130	−4.25	−0.90	−1.70
180	−3.10	−0.63	−1.20
	Channel 20		
130	−3.32	−2.38	−2.46
180	−1.74	−1.73	−1.58

[a] Deviation of brightness temperatures (in K) as would be recorded by sensor (AMSU-B), calculated by MAES, MIRART, and MOLIERE/5 from those calculated by ARTS, for the 5 channels of AMSU-B and the two extreme viewing angles.

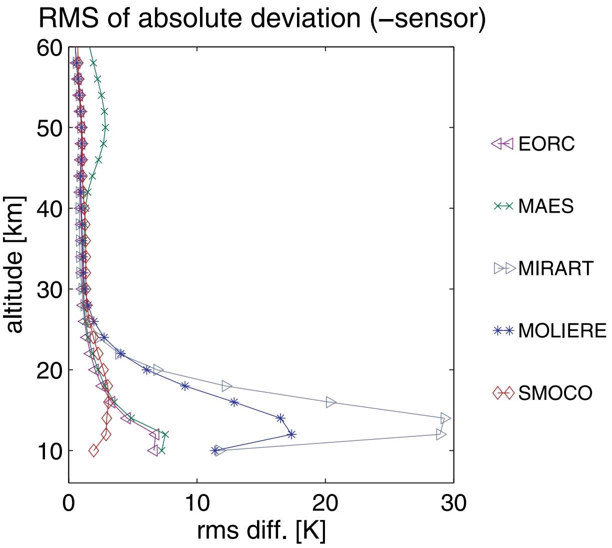

Figure 20. Exercise 4, limb-looking geometry. Root mean square of absolute deviation of spectra as would be recorded by the sensor, from ARTS, as a function of tangent altitude.

[73] At higher altitudes both a shift in the line center frequency and a difference in the line intensities are seen. These are explained by the different spectroscopic data which have been used. For example, at 22 km, in most parts of the spectrum, MOLIERE/5 is about 5 K higher than ARTS, whereas MIRART is about 3 K lower than ARTS. The biggest deviation of about 40 K (MAES) can be seen at 52 km at about 500.44 GHz (Figure 21, right panel). It is probably caused by a shift of the line found at this frequency: The line is so narrow that it will be sampled differently by the frequency grid, resulting in a different peak value. Since the spike is very narrow, it does not have much weight in the root mean square plot (Figure 20). Note that, for limb-looking geometry, neither differences in continuum absorption modeling nor frequency shifts cause much harm in retrieval, as explained below (section 8.6). However, discrepancies coming from the radiative transfer calculations or the instrument model can cause large systematic retrieval errors.

7.4.3. Up-Looking

[74] The models participating in this exercise are ARTS, KMM, MAES, MIRART, and MOLIERE/5. The results for viewing angles of 0° (i.e., zenith) and 60° are shown in Figure 22.

[75] The largest deviation of several K from ARTS is shown by MAES at a viewing angle of 60° where a shift in the line center can be seen (Figure 22, right panel). The different line center frequency is explained by the different line catalogs used by different models. The same feature is observed for MOLIERE/5: a shift in the line center frequency. In addition, MOLIERE/5 is about 3 K higher in the far wings. The deviation in the line wings can be explained by the different continuum absorption models, (N_2, O_2, and H_2O) and the line

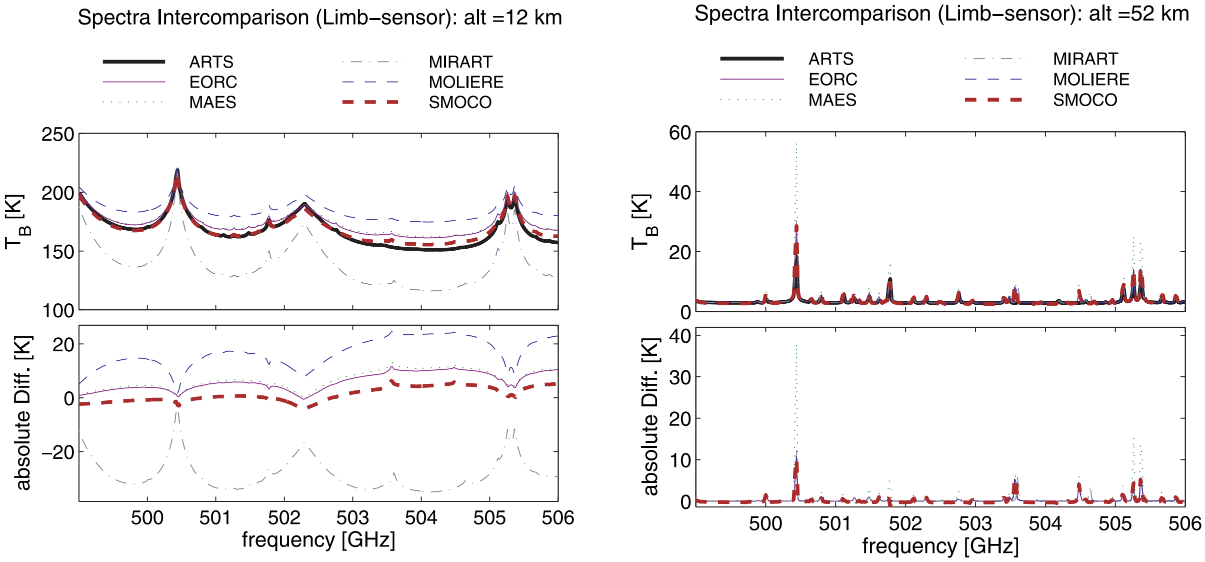

Figure 21. Exercise 4, limb-looking geometry. Top panels show spectra as would be recorded by a sensor, calculated by ARTS, EORC model, MOLIERE/5, MAES, and SMOCO. Bottom panels show absolute deviation from ARTS. Tangent altitude (left) 12 km and (right) 52 km.

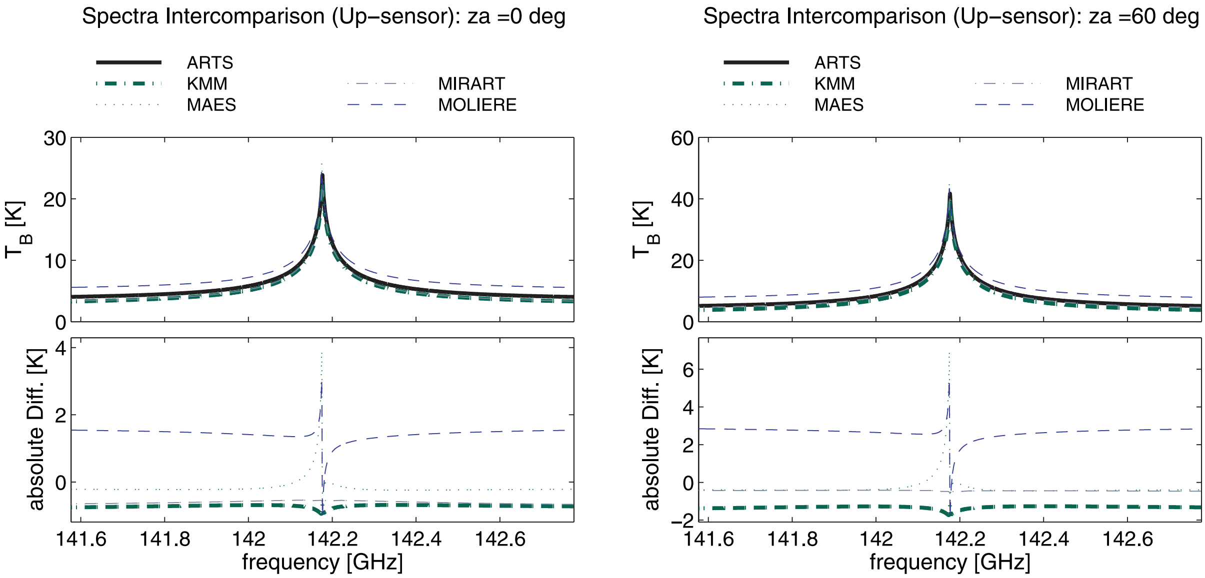

Figure 22. Exercise 4, up-looking geometry. Top panels show spectra as would be recorded by a sensor, calculated by different models. Bottom panels show absolute deviation from ARTS. Viewing angle 0°, i.e., (left) zenith-looking and (right) 60°.

selection of the far out-of-band lines. Apart from that, all differences are of the order of 1 K.

8. Lessons Learned, Summary

[76] The paper so far has presented only the final version of the intercomparison, which was achieved in several iterations over the course of two years. The purpose of this section is to describe the problems that were encountered in the process, as well as to reflect on the lessons that can be learned from this activity.

8.1. The First Try

[77] When the intercomparison was planned, it was clear that it would be necessary to distinguish between actual model differences and differences due to different choices of (sometimes uncertain) model input parameters. Therefore exercise 1 and 3 were set up to test the implementation of absorption calculation and radiative transfer, respectively, and exercise 2 and 4 were set up to test the absolute uncertainties, including uncertainties in model parameter choices.

[78] At the beginning of the intercomparison, detailed descriptions of the exercises were given to the participants. Although the experience from several previous intercomparison activities was used, it turned out that the descriptions were not complete, or could easily be misunderstood. The most prominent model parameters suspected to be causing problems were:

8.1.1. Absorption

[79] 1. Line shape functions, including prefactors.

[80] 2. Self-broadening (included or not).

[81] 3. Possible pressure shift for some lines, e.g., the HCl line at 625.9 GHz.

[82] 4. Errors in the established MPM93 water vapor absorption model, which had been corrected by some participants, but had not been corrected by others.

[83] 5. Different partition functions used to convert line intensities to temperatures other than the catalog reference temperature.

8.1.2. Radiative Transfer

[84] 1. Different interpolation strategies (atmospheric properties as a function of altitude).

[85] 2. Brightness temperature units (Planck versus Rayleigh-Jeans brightness temperatures).

[86] 3. Surface emissivity for the down-looking case.

[87] 4. Misunderstandings in the sensor description.

[88] 5. Cosmic background for up and limb-looking cases.

[89] 6. Handling of refraction.

[90] 7. Exact earth shape model (viewing angles rather than tangent altitudes had been specified for the limb cases, which made the calculations sensitive to the assumed earth radius).

[91] The discrepancies, particularly in the absorption intercomparison, were so large that it was decided to add an additional exercise 0 testing only the line shape. Also,

all remaining unclear model parameters were fixed explicitly for exercises 1 and 3 (brightness temperatures should be Planck, pressure shift should be included, etc.). In the following subsections, the lessons learned from the individual exercises will be discussed in detail.

8.2. Exercise 0

[92] An important lesson learned was that it is essential to start with the simplest possible case, before moving on to more complex cases. It turned out that already in the exercise of simulating absorption only for a single line at the catalog reference temperature with an exactly predefined line shape, that of equation (12), there is some room for bugs and misunderstandings. These were related to formats and units of spectroscopic data and formats and units of output files to be delivered. After these issues were resolved, the agreement between the models was excellent.

[93] The next thing to check with exercise 0 was the implementation of the temperature dependence of the line strength. Differences here come from different approaches for temperature dependence of the partition function, and from implementation differences in the line width and line broadening. It turned out that for the case investigated they can reach up to about 1.5% in the case of one model (BEAM), but are generally much lower.

[94] It should be noted that the partition function depends on molecular species, so errors could be somewhat larger for other species. Nevertheless, our conclusion is that discrepancies resulting from the partition function should normally be well below 1% and therefore be small compared to other uncertainties.

8.3. Exercise 1

8.3.1. Line-by-Line Calculation

[95] Those models that were close in exercise 0 were also close here, as expected. After all model parameters had been tied down and all misunderstanding about units and file formats had been resolved, errors were mostly below 1.5%. This shows that the models work consistently for consistent input and that the line-by-line implementation contains no significant bugs.

8.3.2. Continuum Absorption

[96] Participants were asked to simulate total water vapor absorption from the Liebe MPM93 model. An interesting result of this was that intensities of isotopic water vapor lines in MPM93 are wrong (see section 6.4). This was already known to some participants, but not to others. It seems not to have been documented in the literature so far.

[97] Otherwise this exercise presented no major problems. It should be noted, however, that there is a large uncertainty in the MPM93 model itself. The MPM93 model was just chosen as an example because most participants had already implemented it, not because it is believed to be the most accurate water vapor absorption model. Certainly, the uncertainties within the water vapor absorption model by far exceed the uncertainties in the implementation.

8.4. Exercise 2

[98] When participants are given the choice to implement their own best effort for line spectrum and continuum, differences are much larger, corresponding to about 10% near the center of major absorption lines. In the line wings/window regions, where the absolute value of the absorption coefficient is very small, the same absolute differences correspond to very high relative differences of tens or even hundreds of percent (which is why relative differences are not very meaningful in this context); the same applies for discrepancies of line center frequencies and for absorption lines that are not considered by all models. This confirms that the spectroscopic assumptions are the largest source of uncertainty for the calculation of absorption coefficients. The important uncertain factors are (1) the spectral line database, (2) the line shape function, and (3) continuum absorption modeling. These uncertainties can only be reduced by studies comparing predicted absorption to measured absorption, preferably in the laboratory.

8.5. Exercise 3

[99] There were found to be no fundamental problems with the radiative transfer calculation itself, only interpolation effects, which can lead to brightness temperature differences of up to 3 K for the limb looking geometry. For down and up-looking geometry the differences due to interpolation effects are only up to 0.1 K. How a model interpolates for example the atmospheric temperature between the altitudes where it is given is largely a matter of definition. (The only demand is that it should be clearly documented what the model is doing, so that the user can take it into account when interpreting the results.) To eliminate this problem one has to do the intercomparison for a very fine altitude grid, for which interpolation effects become negligible.

8.6. Exercise 4

[100] With free model parameters, model differences are much larger. They can reach a few K for the up-looking and down-looking geometries, and up to about 20 K for the limb geometry. The source of these discrepancies are the differences in the absorption coefficient, i.e., in the spectroscopy (see section 8.4).

[101] The limb case is peculiar. Because of the long limb path, small differences in the absorption can lead to large differences in brightness temperature. These bright-

ness temperature differences occur particularly in the line wings and in the windows between spectral lines because of the large discrepancies in the continuum between the different models.

[102] Note that differences in continuum modeling do usually not harm retrieval: For up-looking geometry, usually a tropospheric correction is done, based, e.g., on a one-layer model of the troposphere, on an assumption on the mean tropospheric temperature and on the measured brightness temperature in some far line wing or continuum channel. Thus the tropospheric opacity and the emission by the troposphere can be estimated which means that the forward model only needs to deal with the stratosphere, i.e., line absorption/emission. For limb-looking geometry, continuum absorption can be fitted during retrieval, provided the frequency range does not just cover the center of a strong line. Only for the down-looking case is the absolute value of the absorption coefficient, including continuum, critical. Frequency shifts can also be fitted or corrected for in principle, although this is not always easy in practice (S. A. Buehler et al., The expected performance of the SMILES submillimeter-wave limb sounder compared to aircraft data, submitted to *Radio Science*, 2004).

[103] A study by *von Clarmann et al.* [2003a] that compares retrieval results from several data processors showed that despite some deviations of the forward models, retrieved profiles are fairly close and the differences can largely be attributed to different approaches in the inversion process, e.g., regularization, use of a priori data, discretization.

9. Conclusion

[104] The intercomparison of eight clear-sky atmospheric radiative transfer models showed little deviation of model results from each other provided input parameters and parameters governing the algorithm (e.g., the line shape function) are the same. This shows correctness of the numerical implementations, but is not a validation in the strict sense (a real validation can only be done by comparison with measured data). With free input, the spread of the results from the different models (which is an estimate of the modeling error) was about 10% for absorption calculations and a few K for simulated brightness temperatures for up- or down-looking sensors. The cause of such a spread are mainly uncertainties in the spectroscopic data.

[105] Unfortunately, the question which radiative transfer model best fits reality cannot be solved satisfactorily by model comparison. The ultimate test is to measure atmospheric state and radiance spectra simultaneously and then directly compare simulated to measured radiances. This cannot be done for a model in general, but rather individually for each application and configuration. For the case of the down-looking instrument AMSU and the ARTS model, e.g., this has already been done [*Buehler et al.*, 2004].

Appendix A: Relevant Details on the Forward Models

[106] Here we present relevant details of the participating forward models that did not fit into Table 1 (e.g., where there was an “O” for “other” in a table entry).

A1. Atmospheric Radiative Transfer Simulator (ARTS)

[107] Absorption coefficients can be calculated line-by-line from an external spectral line catalog, or they can be calculated by some built-in absorption models. Besides the catalog formats of JPL and HITRAN, the model supports the MYTRAN format, which was defined by *Bauer et al.* [1998], and a native catalog format, as described by *Buehler and Eriksson* [2000].

[108] For the temperature conversion of the line strength, partition functions are calculated from an internal polynomial representation, which is taken from the TIPS-dst97 FORTRAN program [*Gamache et al.*, 2000] for those species included in TIPS. For the other species, a polynomial fit to the tabulated partition function values of JPL is used. Where not even that is available for some isotopic species, the partition function for the main isotope is used.

[109] Further details are in the ARTS User Guide (by S. Buehler et al.; available at http://www.sat.uni-bremen.de/arts/). The following additional continuum absorption models are implemented: the model by *Ma and Tipping* [2002] and the model by *Cruz Pol et al.* [1998].

[110] The radiative transfer is calculated in equal distance steps along the line of sight, assuming a spherically symmetric atmosphere. The absorption coefficients at line-of-sight grid points are interpolated (linearly in log p) from absorption coefficients precalculated on a sufficiently fine pressure grid. Used for the intercomparison was arts-1-0-64.

[111] Note that in an independent exercise [*John et al.*, 2002], ARTS was found to be in very good agreement with a large group of operational radiative transfer models for this sensor type which have been compared in the work of *Garand et al.* [2001]. The bias found for AMSU channel 18 was 0.37 K compared to the reference model of the study by *Garand et al.* [2001]. Bias here means the mean (over a set of atmospheric states) of the difference between brightness temperatures from ARTS and from the reference model, and the criteria for the

quality of the agreement are the ones stated in the latter study.

A2. Bernese Atmospheric Model (BEAM)

[112] BEAM uses an internal spectroscopic database that was originally produced in 1995 from earlier versions of the JPL catalog [*Poynter and Pickett*, 1985] and HITRAN [*Rothman et al.*, 1992]. Today, the BEAMCAT database [*Feist*, 2004, 1999b] can be used to produce merged database files from the most recent versions of these catalogs [*Pickett et al.*, 1998; *Rothman et al.*, 1998].

[113] Line strength at a given temperature is calculated by linearly interpolating the logarithms of the rotational partition functions at 150, 225, and 300 K (as listed, for example, in the JPL catalog) versus the logarithm of temperature. Unlike many of the other models, BEAM is a pure spectroscopic model that calculates only absorption coefficients, not radiative transfer.

A3. EORC Model

[114] For the temperature conversion of the line strength, the rotation-spin partition functions at any temperature are computed by interpolating data at 150, 225, and 300 K which are taken from the JPL catalog. A linear fit is adopted for the logarithm of the ratio of partition functions with respect to the logarithm of the temperature. However, it is also possible to select a quadratic polynomial fit or a classical approximation of the partition functions. Currently the electronic-vibrational partition functions are simply set to 1. This means their contributions are not estimated correctly unless they are included in the rotation-spin partition functions in the catalog. In the assumption of spherical symmetry, the atmosphere is divided into spherical layers and the absorption coefficients are calculated at the boundaries of each layer in the line-by-line manner.

[115] For all observation geometries, this single layering is used for integrating the radiative transfer equation recursively. The thickness of each layer should be small enough to guarantee numerical accuracy and is determined by the user by taking the numerical efficiency into account. Antenna integration, convolution with the instrument line shape function, and some other functions which are useful for simulating the forward processes in heterodyne receivers are supported.

A4. Karlsruhe Millimeter-Wave Forward Model (KMM)

[116] The ratio of the partition functions $Q(T_0)/Q(T)$ used in the temperature conversion of the line strength (see equation (5)) is approximated by

$$\frac{Q(T_0)}{Q(T)} = \frac{T_0}{T} \tag{A1}$$

for linear molecules and

$$\frac{Q(T_0)}{Q(T)} = \left(\frac{T_0}{T}\right)^{3/2} \tag{A2}$$

for asymmetric molecules, respectively, as suggested in *Janssen* [1993].

[117] In the radiative transfer calculations the inhomogeneity of the atmosphere is taken into account by the use of Curtis-Godson means (see equation (11)) of the layers, for the pressure, temperature, and volume mixing ratios. Not included in the forward model are the pressure shift, antenna pattern, and channel characteristics of the spectrometer.

A5. Millimeter Wave Atmospheric Emission Simulator (MAES)

[118] Retrieval calculations are not included in the MAES code. MAES can be used with separately developed retrieval codes. The Voigt line shape function is calculated by simple integration. This integration is accurate but not as computationally efficient as other approximations like the one by *Hui et al.* [1978]. However, since the altitude range where the Voigt function is required is limited for the typical application of MAES like stratospheric limb sounding, the disadvantage by the increased computational demand is negligible.

[119] The brightness temperature is obtained by integrating the radiative transfer equation. MAES simply integrates the equation by summing up the integrands computed at every grid point along the line of sight. The grid is iteratively divided into a finer grid until the integration result converges. The absorption coefficient is interpolated at each grid point from absorption coefficients calculated in advance at a sparse height grid. Analytical Jacobians can also be calculated in MAES.

A6. Modular Infrared Atmospheric Radiative Transfer (MIRART)

[120] Apart from the HITRAN and JPL spectral line catalogs, line parameters from HiTemp [*Rothman et al.*, 1995], SAO [*Chance et al.*, 1994], or GEISA [*Jacquinet-Husson et al.*, 1999] spectral line catalogs can be used in MIRART.

[121] The temperature conversion of the line strength follows the scheme used in the ATMOS software [*Norton and Rinsland*, 1991]. For the calculation of the Voigt line shape function, MIRART uses an optimized combination of the Humlicek [*Humlicek*, 1982] and Hui-Armstrong-Wray [*Hui et al.*, 1978] complex

error function algorithm [*Schreier*, 1992] and switches to pure Lorentz line shape in the far wings; a further optimization similar in spirit to the work of *Kuntz* [1997] exploits the equidistant wave number grid. The wave number grid is chosen individually for each altitude level and molecule. Furthermore a coarse grid is used for contributions of lines outside the spectral region of interest, whereas contributions near the line center are calculated on a fine spectral grid. Additional continuum absorption model: an empirical continuum for the far infrared provided by K. Chance (private communication, 1996) can be used.

[122] The solution of the radiative transfer equation and the Lambert-Beer law requires the integration of spatially varying quantities which are given only for a set of discrete altitude points along the line of sight. These integrals are, in contrast to the Curtis-Godson approach or weighted means over each layer (see equation (11)), calculated using standard numerical quadrature schemes. MIRART has implemented a trapezoid quadrature scheme, the method of overlapping parabolas, and a piecewise cubic Hermite quadrature [*Kahaner et al.*, 1989]. Note that in addition to the present intercomparison MIRART was also extensively cross-checked in the framework of the AMIL2DA project [*von Clarmann et al.*, 2003a, 2003b].

A7. Microwave Observation Line Estimation and Retrieval Code (MOLIERE/5)

[123] Spectroscopic line parameters are taken from the Verdandi line catalog [*Eriksson*, 1999] which is basically a merge of JPL line catalog data with line broadening parameters (mainly from the HITRAN line catalog). By converting to Verdandi format, the JPL, HITRAN and MYTRAN [*Bauer et al.*, 1998] line catalogs can also be used.

[124] The ratio of the partition functions $Q(T_0)/Q(T)$ used in the temperature conversion of the line strength (see equation (5)) is approximated as a third-order polynomial. The standard coefficients are based on a polynomial fit to JPL values for a range of atmospheric temperatures. Intensities, given in JPL units in Verdandi, are converted to any temperature using the formulation provided by the JPL catalog. Absorption calculation includes pressure shift as described by *Pumphrey and Buehler* [2000]. The CO_2 continuum absorption is parameterized according to *Rosenkranz* [1993]. Refractive indices, which are used to correct the radiation path for the effects of refraction, are obtained from MPM93. For this intercomparison study, MOLIERE/4.98 was used, which is identical to MOLIERE/5 in the modules relevant here (spectroscopy, radiative transfer, instrumental functions).

A8. SMILES Observation Retrieval Code (SMOCO)

[125] The integration of the radiative transfer is done iteratively for speed-up. SMOCO can deal with an asymmetric atmosphere that has different molecular mixing ratios in farther and nearer regions from the tangent point along the line of sight. Note that SMOCO is very similar to MAES. Their differences are: (1) SMOCO uses Kuntz's approximation [*Kuntz*, 1997] to calculate the Voigt line shape function while MAES uses a much simpler integration for it, (2) SMOCO integrates the radiative transfer equation using an iterative approach while MAES integrates directly. The main reason for these differences is that SMOCO, being the retrieval code for the ground segment of SMILES, has to put emphasis on speed.

[126] **Acknowledgments.** The development of ARTS was funded by the German Federal Ministry of Education and Research (BMBF), within the AFO2000 project UTH-MOS, grant 07ATC04, and the DLR project SMILES, grant 50EE9815. It is a contribution to COST Action 723 "Data Exploitation and Modeling for the Upper Troposphere and Lower Stratosphere." The development of MOLIERE-5 by J. Urban was indirectly supported by grants from the European Space Agency, ESA/ESTEC contract 11979/97/NL/CN, CCN 2 of the "Study on the Retrieval of Data from Submillimeter Limb Sounding" and by contracts from the Centre National d'Études Spatiales (CNES). Work on the MIRART code by F. Schreier was partially supported within the AMIL2DA project, a shared cost action within the RTD generic activities of the 5th FP EESD Programme of the European Commission, project EVG1-CT-1999-00015. The model intercomparison described in this paper was the main topic of the "Third International Radiative Transfer Modeling Workshop," which took place from 10 to 11 October 2001 at the Hanse Wissenschaftskolleg, Delmenhorst, Germany. A substantial portion of the discussion during the conduction of the study and of the writing of this paper took place during the Fourth and Fifth International Radiative Transfer Modeling Workshops in Bredbeck, Germany, in July 2002 and 2003. We gratefully acknowledge the funding of all of these workshops by DLR in the framework of the project SMILES, grant 50EE9815.

References

Anderson, G., S. Clough, F. X. Kneizys, and E. Shettle (1986), AFGL atmospheric constituents (1 – 120 km), *Tech. Rep. TR-86-0110*, Air Force Geophys. Lab., Bedford, Mass.

Bauer, A., M. Godon, M. Kheddar, and J. M. Hartmann (1989), Temperature and perturber dependence of water vapor line broadening: Experiments at 183 GHz, calculations below 1000 GHz, *J. Quant. Spectrosc. Radiat. Transfer*, *41*, 49–54.

Bauer, A., M. Birk, S. Buehler, J. Colmont, A. von Engeln, K. Künzi, A. Perrin, D. Priem, G. Wagner, and G. Wlodarczak (1998), Study on a spectroscopic database for millimeter and submillimeter wavelengths, final report, *Tech. Rep.*, *Contract 11581-95-NL-CN*, Eur. Space Res. and Technol. Cent., Noordwijk, Netherlands.

Buehler, S., and P. Eriksson (Eds.) (2000), *Atmospheric Millimeter and Sub-Millimeter Wave Radiative Transfer Modeling*, Ber. aus der Phys., Shaker Verlag GmbH, Aachen, Germany.

Buehler, S. A., M. Kuvatov, V. O. John, U. Leiterer, and H. Dier (2004), Comparison of microwave satellite humidity data and radiosonde profiles: A case study, *J. Geophys. Res.*, *109*, D13103, doi:10.1029/2004JD004605.

Buehler, S. A., P. Eriksson, T. Kuhn, A. von Engeln, and C. Verdes (2005), ARTS, The atmospheric radiative transfer simulator, *J. Quant. Spectrosc. Radiat. Transfer*, *91*, 65–93, doi:10.1016/j.jqsrt.2004.05.051.

Chance, K., K. Jucks, D. Johnson, and W. A. Traub (1994), The Smithsonian Astrophysical Observatory database 1992, *J. Quant. Spectrosc. Radiat. Transfer*, *52*, 447–457.

Clough, S., F. Kneizys, and R. Davies (1989), Line shape and the water vapor continuum, *Atmos. Res.*, *23*, 229–241.

Cruz Pol, S. L., C. S. Ruf, and S. J. Keihm (1998), Improved 20–32 GHz atmospheric absorption model, *Radio Sci.*, *33*, 1319–1333.

Eriksson, P. (1999), Microwave radiometric observations of the middle atmosphere: Simulations and inversions, Ph.D. thesis, Chalmers Univ. of Technol., Göteborg, Sweden.

Feist, D. G. (1999a), Analysis and simulation of atmospheric microwave spectra measured with a space borne limb-sounding instrument, Ph.D. thesis, Univ. of Bern, Bern.

Feist, D. G. (1999b), BEAMCAT 1.0: A spectral line database for millimeter and submillimeter wave propagation in the Earth's atmosphere, *Tech. Rep. 99-1*, Inst. of Appl. Phys., Bern.

Feist, D. G. (2001), *The Bernese Atmospheric Model (BEAM),* in *Atmospheric Millimeter and Sub-Millimeter Wave Radiative Transfer Modeling II: Proceedings of the Second International Workshop on Millimeter and Sub-Millimeter Wave Radiative Transfer Modeling, Held at Haus Bredbeck, Germany, June 19–22, 2000*, *Ber. Inst. Umweltphys.*, vol. 4, chap. 1, pp. 13–22, Logos Verlag, Berlin.

Feist, D. G. (2004), The Bernese Atmospheric Multiple Catalog Access Tool (BEAMCAT): A tool for users of popular spectral line catalogs, *J. Quant. Spectrosc. Radiat. Transfer*, *85*(1), 57–97.

Feist, D. G., and N. Kämpfer (1998), BEAM: A fast versatile model for atmospheric absorption coefficients from 0–1000 GHz, *Proc. SPIE Int. Soc. Opt. Eng.*, *3503*, 301–312.

Gamache, R. R., S. Kennedy, R. Hawkins, and L. S. Rothman (2000), Total internal partition sums for molecules in the terrestrial atmosphere, *J. Mol. Struct.*, *517-518*, 407–425.

Garand, L., et al. (2001), Radiance and Jacobian intercomparison of radiative transfer models applied to HIRS and AMSU channels, *J. Geophys. Res.*, *106*, 24,017–24,031.

Goody, R. M., and Y. L. Yung (1989), *Atmospheric Radiation, Theoretical Basis*, 2nd ed., Oxford Univ. Press, New York.

Hui, A., B. Armstrong, and A. Wray (1978), Rapid computation of the Voigt and complex error functions, *J. Quant. Spectrosc. Radiat. Transfer*, *19*, 509–516.

Humlicek, J. (1982), Optimized computation of the Voigt and complex probability function, *J. Quant. Spectrosc. Radiat. Transfer*, *27*, 437–444.

Irimajiri, Y., et al. (2002), A balloon-borne superconducting receiver at 650-GHz band, *Singapore J. Phys.*, *18*(1), 177–180.

Jacquinet-Husson, N., et al. (1999), The 1997 spectroscopic GEISA databank, *J. Quant. Spectrosc. Radiat. Transfer*, *62*, 205–254.

Janssen, M. A. (Ed.) (1993), *Atmospheric Remote Sensing by Microwave Radiometry*, John Wiley, Hoboken, N. J.

John, V. O., M. Kuvatov, and S. A. Buehler (2002), ARTS—A new radiative transfer model for AMSU, paper presented at Twelfth International TOVS Study Conference (ITSC-XII), Bur. of Meteorol. Res. Cent., Melbourne, Vict., Australia.

Kahaner, D., C. Moler, and S. Nash (1989), *Numerical Methods and Software*, Prentice-Hall, Upper Saddle River, N. J.

Kopp, G. (2001), The Karlsruhe millimeterwave forward model, in *Atmospheric Millimeter and Sub-Millimeter Wave Radiative Transfer Modeling II: Proceedings of the Second International Workshop on Millimeter and Sub-Millimeter Wave Radiative Transfer Modeling, Held at Haus Bredbeck, Germany, June 19–22, 2000*, *Ber. Inst. Umweltphys.*, vol. 4, pp. 25–31, Logos Verlag, Berlin.

Kuhn, T. (2004), Atmospheric absorption models for the millimeter wave range, Ph.D. thesis, Univ. of Bremen, Bremen, Germany.

Kuntz, M. (1997), A new implementation of the Humlicek algorithm for the calculation of the Voigt profile function, *J. Quant. Spectrosc. Radiat. Transfer*, *57*, 819–824.

Langer, J., U. Klein, K. F. Künzi, U. Raffalski, and B.-M. Sinnhuber (1996), A versatile millimeter wave radiometer for spectroscopic measurements of atmospheric trace gases, in *Proceedings of the XVIII Quadrennial Ozone Symposium, L'Aquila, Italy*, edited by A. Bojkov and G. Visconti, pp. 931–934, Edigrafital, S. Atto, Italy.

Liebe, H. J. (1985), An updated model for millimeter wave propagation in moist air, *Radio Sci.*, *20*, 1069–1089.

Liebe, H. J. (1989), MPM—An atmospheric millimeter-wave propagation model, *Int. J. Infrared Millimeter Waves*, *10*(6), 631–650.

Liebe, H. J., G. Hufford, and M. Cotton (1993), Propagation modeling of moist air and suspended water/ice particles at frequencies below 1000 GHz, paper presented at 52nd Specialists Meeting of the Electromagnetic Wave Propagation Panel, Advis. Group for Aerosp. Res. and Devel., Mallorca, Spain.

Ma, Q., and R. H. Tipping (2002), Water vapor millimeter wave foreign continuum: A lanczos calculation in the coordinate representation, *J. Chem. Phys.*, *117*(23), 10,581–10,596, doi:10.1063/1.1516792.

Norton, R., and C. Rinsland (1991), ATMOS data processing and science analysis methods, *Appl. Opt.*, *30*, 389–400.

Ochiai, S., Y. Irimajiri, and H. Masuko (2001), 270 GHz SIS radiometer for stratospheric ClO observation, in *Proc. SPIE Int. Soc. Opt. Eng.*, *4152*, 372–379.

Pickett, H. M., R. L. Poynter, and E. A. Cohen (1992), Submillimeter, millimeter, and microwave spectral line catalogue, *Tech. Rep. 80–23*, *Rev. 3*, Jet Propul. Lab., Pasadena, Calif.

Pickett, H., R. Poynter, E. Cohen, M. Delitsky, J. Pearson, and H. Müller (1998), Submillimeter, millimeter, and microwave spectral line catalog, *J. Quant. Spectrosc. Radiat. Transfer*, *60*, 883–890.

Poynter, R. L., and H. M. Pickett (1985), Submillimeter, millimeter, and microwave spectral line catalog, *Appl. Opt.*, *24*(14), 2235–2240.

Pumphrey, H., and S. Buehler (2000), Instrumental and spectral parameters: Their effect on an measurement by microwave limb-sounding of the atmosphere, *J. Quant. Spectrosc. Radiat. Transfer*, *64*, 421–437.

Rayer, P. (2001), The VVH and VVW spectral functions, in *Atmospheric Millimeter and Sub-Millimeter Wave Radiative Transfer Modeling II: Proceedings of the Second International Workshop on Millimeter and Sub-Millimeter Wave Radiative Transfer Modeling, Held at Haus Bredbeck, Germany, June 19–22, 2000*, *Ber. Inst. Umweltphys.*, vol. 4, edited by P. Eriksson and S. Buehler, pp. 131–160, Logos Verlag, Berlin.

Reburn, W. J., R. Siddans, B. J. Kerridge, S. Bühler, A. von Engeln, P. Eriksson, T. Kuhn, K. Künzi, and C. Verdes (2000), Critical assessments in millimetre-wave atmospheric limb sounding, *Fin. Rep. Contract 13348/98/NL/GD*, Eur. Space Res. and Technol. Cent., Noordwijk, Netherlands.

Rosenkranz, P. (1993), Absorption of microwaves by atmospheric gases, in *Atmospheric Remote Sensing by Microwave Radiometry*, edited by M. Janssen, chap. 2, John Wiley, Hoboken, N. J.

Rosenkranz, P. W. (1998), Water vapor microwave continuum absorption: A comparison of measurements and models, *Radio Sci.*, *33*(4), 919–928. (Correction in *Radio. Sci.*, *34*, 1025, 1999.)

Rothman, L., et al. (1992), The HITRAN molecular database: Editions of 1991 and 1992, *J. Quant. Spectrosc. Radiat. Transfer*, *48*(5/6), 469–507.

Rothman, L. S., R. Wattson, R. R. Gamache, J. W. Schroeder, and A. McCann (1995), HITRAN HAWKS and HITEMP high temperature molecular database, in *Proc. SPIE Int. Soc. Opt. Eng.*, *2471*, 105–111.

Rothman, L., et al. (1998), The HITRAN molecular spectroscopic database and HAWKS (Hitran Atmospheric Workstation): 1996 edition, *J. Quant. Spectrosc. Radiat. Transfer*, *60*(5), 665–710.

Schreier, F. (1992), The Voigt and complex error function: A comparison of computational methods, *J. Quant. Spectrosc. Radiat. Transfer*, *48*, 743–762.

Schreier, F., and U. Böttger (2003), MIRART, a line-by-line code for infrared atmospheric radiation computations including derivatives, *Atmos. Oceanic Opt.*, *16*, 262–268.

Schreier, F., and B. Schimpf (2001), A new efficient line-by-line code for high resolution atmospheric radiation computations including derivatives, in *IRS 2000: Current Problems in Atmospheric Radiation*, edited by W. Smith and Y. Timofeyev, pp. 381–384, A. Deepak, Hampton, Va.

Schwartz, M. J. (1997), Observation and modeling of atmospheric oxygen millimeter-wave transmittance, Ph.D. thesis, Mass. Inst. of Technol., Cambridge, Mass.

SMILES Mission Team (2002), JEM/SMILES mission plan, Earth Sci. Technol. Off., Goddard Space Flight Cent., Greenbelt, Md.

Tjemkes, S., et al. (2003), The isswg line-by-line inter-comparison experiment, *J. Quant. Spectrosc. Radiat. Transfer*, *77*(4), 433–453.

Urban, J., P. Baron, N. Lautié, K. Dassas, N. Schneider, P. Ricaud, and J. de La Noë (2004), Moliere (v5): A versatile forward and inversion model for the millimeter and sub-millimeter wavelength range, *J. Quant. Spectrosc. Radiat. Transfer*, *83*(3–4), 529–554.

Vangasse, P., J. Charlton, and M. Jarrett (1995), Characterization of the advanced microwave sounding unit, AMSU-B, *Adv. Space Res.*, *17*(1), 75–78.

Van Vleck, J. H., and V. F. Weisskopf (1945), On the shape of collision-broadened lines, *Rev. Mod. Phys.*, *17*(2–3), 227–236.

von Clarmann, T., et al. (2003a), A blind test retrieval experiment for infrared limb emission spectrometry, *J. Geophys. Res.*, *108*(D23), 4746, doi:10.1029/2003JD003835.

von Clarmann, T., et al. (2003b), Modeling of atmospheric mid-infrared radiative transfer: The AMIL2DA algorithm intercomparison experiment, *J. Quant. Spectrosc. Radiat. Transfer*, *78*, 381–407.

S. A. Buehler, C. Emde, V. O. John, N. Koulev, O. Lemke, C. Melsheimer, T. R. Sreerekha, and C. Verdes, Institute of Environmental Physics, University of Bremen, NW1, Otto-Hahn-Allee 1, D-28359 Bremen, Germany. (sbuehler@uni-bremen.de; claudia@sat.physik.uni-bremen.de; vojohn@uni-bremen.de; nkoulev@uni.bremen.de; olemke@uni-bremen.de; melsheimer@uni-bremen.de; rekha@uni-bremen.de; cverdes@sat.physik.uni-bremen.de)

P. Eriksson and J. Urban, Department of Radio and Space Science Chalmers University of Technology, Hörsalsvägen 11, SE-41296 Göteborg, Sweden. (patrick.eriksson@rss.chalmers.se; jo.urban@rss.chalmers.se)

D. G. Feist, Institute of Applied Physics, University of Bern, Sidlerstrasse 5, CH-3012 Bern, Switzerland. (dietrich.feist@mw.iap.unibe.ch)

S. Ichizawa and M. Suzuki, Earth Observation Research and Application Center, Japan Aerospace Exploration Agency, Harumi Island Triton Square Office Tower X 23F, 1-8-10

Harumi, Chuo-ku, Tokyo 104-6023, Japan. (ichizawa@eorc.jaxa.jp; suzuki@eorc.jaxa.jp)

Y. Kasai, S. Ochiai, and S. Tsujimaru, SMILES Group, National Institute of Information and Communications Technology (NICT), Koganei, Tokyo 184-8795, Japan. (ykasai@nict.go.jp; ochiai@nict.go.jp; tsujimaru@nict.go.jp)

G. Kopp, Institut für Meteorologie und Klimaforschung, Forschungszentrum Karlsruhe GmbH, P.O. Box 3640, D-76021 Karlsruhe, Germany. (gerhard.kopp@imk.fzk.de)

T. Kuhn, I. Physikalisches Institut, Universität zu Köln, Zülpicher Strasse 77, D-50937 Köln, Germany. (kuhn@ph1.uni-koeln.de)

F. Schreier, German Aerospace Center (DLR), Remote Sensing Technology Institute, Oberpfaffenhofen, D-82234 Wessling, Germany. (franz.schreier@dlr.de)

C. Takahashi, Fujitsu FIP Corporation, System Dept., Environmental System Business Division, Time24 Building, Aomi Koto-ku, Tokyo 135-8686, Japan. (takahashi.c@fip.fujitsu.com)